

Variability of the Atlantic meridional overturning circulation in the last millennium and two IPCC scenarios

Pablo Ortega · Marisa Montoya · Fidel González-Rouco · Juliette Mignot · Stephanie Legutke

Received: 28 December 2010 / Accepted: 19 April 2011
© Springer-Verlag 2011

Abstract The variability of the Atlantic meridional overturning circulation (AMOC) is investigated in several climate simulations with the ECHO-G atmosphere-ocean general circulation model, including two forced integrations of the last millennium, one millennial-long control run, and two future scenario simulations of the twenty-first century. This constitutes a new framework in which the AMOC response to future climate change conditions is addressed in the context of both its past evolution and its natural variability. The main mechanisms responsible for the AMOC variability at interannual and multidecadal time scales are described. At high frequencies, the AMOC is directly responding to local changes in the Ekman transport, associated with three modes of climate variability: El Niño-Southern Oscillation (ENSO), the North Atlantic Oscillation (NAO), and the East Atlantic (EA) pattern. At low frequencies, the AMOC is largely controlled by

convection activity south of Greenland. Again, the atmosphere is found to play a leading role in these variations. Positive anomalies of convection are preceded in 1 year by intensified zonal winds, associated in the forced runs to a positive NAO-like pattern. Finally, the sensitivity of the AMOC to three different forcing factors is investigated. The major impact is associated with increasing greenhouse gases, given their strong and persistent radiative forcing. Starting in the Industrial Era and continuing in the future scenarios, the AMOC experiences a final decrease of up to 40% with respect to the preindustrial average. Also, a weak but significant AMOC strengthening is found in response to the major volcanic eruptions, which produce colder and saltier surface conditions over the main convection regions. In contrast, no meaningful impact of the solar forcing on the AMOC is observed. Indeed, solar irradiance only affects convection in the Nordic Seas, with a marginal contribution to the AMOC variability in the ECHO-G runs.

P. Ortega (✉) · M. Montoya · F. González-Rouco
Dpto. Astrofísica y Ciencias de la Atmósfera/Instituto de Geociencias, Facultad de Ciencias Físicas, Universidad Complutense de Madrid, Ciudad Universitaria, 28040 Madrid, Spain
e-mail: portegam@fis.ucm.es

P. Ortega · M. Montoya · F. González-Rouco
Instituto de Geociencias (UCM-CSIC), Facultad de Ciencias Físicas, Universidad Complutense de Madrid, Ciudad Universitaria, 28040 Madrid, Spain

J. Mignot
IPSL/LOCEAN, UPMC/CNRS/IRD/MNHN,
Université Pierre et Marie Curie, 4 place Jussieu,
75252 Paris Cedex 05, France

S. Legutke
Deutsches Klimarechenzentrum (DKRZ),
Bundesstrasse 54a, 20146 Hamburg, Germany

Keywords Atlantic meridional overturning circulation · Future climate change · Multidecadal variability · Forced millennial simulations

1 Introduction

The Atlantic meridional overturning circulation (AMOC) is a key factor in understanding the climate of the Northern Hemisphere by virtue of its role in the Earth's energy balance and its contribution to climate variability. Atlantic northward ocean heat transport peaks at about 1 PW (10^{15} W) in the northern tropics (e.g. Trenberth and Caron 2001). A substantial amount of this heat is conveyed by the deep and intermediate overturning circulation (e.g. Talley 2003), which thereby contributes to temper the climate in

northwestern Europe. Through its interaction with the atmosphere, the AMOC has been shown to account for a significant part of surface variability on interannual and, to a larger extent, on decadal and multidecadal time scales. A number of studies suggest an active role of the AMOC in shaping Atlantic and Pacific multidecadal variability (Delworth and Mann 2000; Kerr 2000; Wu and Gordon 2002; Sutton and Hodson 2003; Dong et al. 2006). The AMOC is thought to be linked to the Atlantic multidecadal oscillation (Kushnir 1994; Delworth and Mann 2000; Kerr 2000; Knight et al. 2005), which has in turn been related to widespread regional multidecadal variability (Knight et al. 2006). Furthermore, climate model studies suggest that Atlantic sea surface temperatures (SSTs) are linked to decadal and interdecadal variations of the North Atlantic Oscillation (NAO; Wu and Gordon 2002; Sutton and Hodson 2003), and contribute as well to a multidecadal modulation of El Niño–Southern Oscillation (ENSO) variance (Dong et al. 2006). Likewise, Timmermann et al. (2007) and Dong and Sutton (2007) report enhanced ENSO interannual variability and stronger asymmetry between El Niño and La Niña events as a response to a weakening in the AMOC strength.

Given the evidence that the AMOC may contribute to climate variability at multiple time scales, there is increasing interest in understanding the origins of its variability and investigating its possible response to climate change conditions. Natural AMOC variability has been widely studied through the use of control simulations under current climate conditions performed with atmosphere–ocean general circulation models (AOGCMs; Delworth et al. 1993; Timmermann et al. 1998; Delworth and Greatbatch 2000; Vellinga and Wu 2004; Latif et al. 2004; Dong and Sutton 2005; Knight et al. 2005; Jungclaus et al. 2005; Mignot and Frankignoul 2005; Hawkins and Sutton 2007). These studies have led to the identification of several modes of ocean variability operating from interannual to centennial time scales. AMOC interannual variability is found to be mainly dominated by surface wind–stress variations, through changes in both the Ekman transport and the vertical shear of the meridional flow (Eden and Willebrand 2001; Vellinga and Wu 2004; Mignot and Frankignoul 2005; Hirschi et al. 2007; Cabanes et al. 2008). These wind variations are in turn related to modes of atmosphere variability like NAO and ENSO. In contrast, interdecadal to centennial variability in the AMOC is characterised by a delayed response of the overturning, usually forced by near surface density anomalies in the North Atlantic deep water formation (DWF) regions (e.g. Delworth et al. 1993; Timmermann et al. 1998; Delworth et al. 2002; Dong and Sutton 2005). The origin of these anomalies differs from one model to another, also producing differences in the dominant time scales of AMOC variability. For instance, Delworth et al. (1993) presented a 50-year damped oscillation in a 600-year control simulation

with the GFDL model, in which a weakening of the AMOC was found to lead to lower temperatures in the subpolar North Atlantic, thereby enhancing density in the region and leading to a strengthening of the subpolar gyre. The strengthened subpolar gyre contributed in turn to increase the transport of salinity anomalies to the convection region, thus establishing a mechanism for phase reversal. This mechanism was later found as well by Dong and Sutton (2005) in a 1000-year control run with the HadCM3 model, albeit with a shorter time scale (25 years). A complementary analysis with an extended 1,600 year long version of the same HadCM3 control run was performed by Vellinga and Wu (2004) to identify centennial oscillations. They found a secular mode in which variations in the AMOC strength led to shifts in the Intertropical Convergence Zone (ITCZ) location and thereby to the formation of tropical salinity anomalies. These anomalies were subsequently advected to the North Atlantic, causing a lagged response of the AMOC that contributed to restore the initial ITCZ position. A different multidecadal mechanism has been observed in the same HadCM3 control run (Hawkins and Sutton 2007) as well as in a 500 year control simulation with the ECHAM5/MPI-OM model (Jungclaus et al. 2005). Both simulations identify an internal mode with overturning variability driven by freshwater discharges from the Arctic Ocean that modulate the convective activity in the deep water formation regions. In the HadCM3 model, convection happens most actively in the Nordic Seas region and generates overturning variability in a range of time scales, from multidecadal to centennial. In the ECHAM5/MPI-OM simulation most deep convection variability takes place near the Labrador Sea, where the freshwater export from the Arctic leads to a fluctuation of 70–80 years. Finally, Guemas and Salas-Méllia (2008) have analysed a 400 year long preindustrial control simulation with the CNRM-CM3 model, where the overturning strength also responds to North Atlantic convective forcing on time scales of 5–10 years. They find that convection variability is controlled by the NAO in the Labrador Sea, and is favoured by intensified northerly winds in the Nordic and Irminger Seas. A summary and comparison of the main modes of North Atlantic multidecadal variability in both observations and simulations can be found in Frankcombe et al. (2010).

At the end of the spectrum, studies addressing multi-centennial AMOC variability in the context of an externally-forced climate are scarce (e.g. Hofer et al. 2011). Since there is a sizeable contribution of the AMOC to climate variability in multidecadal time scales, progress in understanding its dynamics may be important for the assessment of decadal predictability and also in discriminating anthropogenic climate change from natural climate variability in the next decades (Dong and Sutton 2005; Keenlyside et al. 2008). A related question is whether and

how the overturning circulation is expected to change under an externally forced climate. This has been intensively addressed in the context of future scenario climate change simulations driven by increasing greenhouse gas (GHG) concentrations (Cubasch et al. 2001; Thorpe et al. 2001; Gregory et al. 2005; Schmittner et al. 2005; Meehl et al. 2007; Drijfhout and Hazeleger 2007; Drijfhout et al. 2008). According to most simulations (Cubasch et al. 2001; Meehl et al. 2007), temperature and precipitation are expected to increase at high-latitudes of the Northern Hemisphere throughout the twenty-first century, both likely contributing to a weakening of the AMOC. In fact, all the experiments including an increase of anthropogenic emissions support this weakening, although none of them simulates a complete collapse by the end of the current century (Gregory et al. 2005; Schmittner et al. 2005; Meehl et al. 2007). Another feature observed in some future scenario projections is a shallowing of the overturning cell that is simultaneous to a northward shift of DWF regions (Drijfhout et al. 2008). In comparison, the influence of other forcing factors (e.g. volcanic aerosols and solar irradiance) on the AMOC is less documented, and the magnitude of its potential impact remains unclear (Zorita et al. 2004; Stendel et al. 2006; Stenchikov et al. 2009; Swingedouw et al. 2010; Ottera et al. 2010).

Here, the variability of the AMOC is analysed in a 1000-year long control run, two forced experiments of the last millennium driven by estimations of natural and anthropogenic factors, and also two future climate change scenario simulations. This provides a new perspective by which future simulated changes of the ocean circulation can be placed in a broader temporal context. The mechanisms responsible for the AMOC variability at interannual and longer time-scales are explored in the available suite of model experiments. Besides, the response to changes in the external forcing is investigated, with a special emphasis on the AMOC and other related quantities. This is done by focusing on the particular influence of each forcing factor.

The paper is organised as follows: Sect. 2 gives a description of the model and the simulations. A first temporal and spatial intercomparison among simulations is addressed in Sect. 3. Sections 4 and 5 describe the main features of AMOC variability at interannual and interdecadal time scales, respectively. The AMOC response to the different forcing factors is presented in Sect. 6. Finally, the main conclusions are summarised in Sect. 7.

2 Model and experiments

This study leans on the analysis of several climate simulations performed with the ECHO-G AOGCM. The ECHO-G model (Legutke and Voss 1999) consists of the spectral

atmospheric model ECHAM4 (Roeckner et al. 1996) and the ocean model HOPE-G (Wolff et al. 1997). Its atmospheric component is set up with a T30 horizontal resolution (ca. $3.75^\circ \times 3.75^\circ$) and 19 vertical levels extending up to 10 hPa, with five of them located above 100 hPa. The horizontal resolution of the ocean model is about $2.8^\circ \times 2.8^\circ$, with an enhancement of the meridional resolution in the Tropics and towards the Equator, where it reaches a minimum grid point separation of 0.5° . This refinement in resolution is intended to provide a more realistic representation of equatorial and tropical ocean currents. Vertical discretisation of the ocean incorporates 20 variably spaced levels, 14 of which are located in the upper 1,000 m. To avoid climate drift, the ocean component includes both heat and freshwater flux adjustments. The same corrections are applied to all experiments analysed in this study. They are diagnosed as annual mean values from the relaxation terms during the last 100 years of a coupled spin-up phase which preceded the control experiment. In that spin-up phase, SST was relaxed to monthly climatological values calculated from the Atmospheric Model Intercomparison Project (AMIP) data for 1979–1994 (Gates 1992) assuming a relaxation constant of $40 \text{ W/m}^2 \text{ K}$. Sea surface salinity is relaxed to seasonal climatological values (Levitus et al. 1994) on a time scale of 30 days. No salinity relaxation is applied in the climatological sea-ice regions as diagnosed from the AMIP SST to avoid distortion of the upper salinity changes related with sea-ice production. Both flux fields are normalized to vanish globally. With this flux correction method the wind-stress, which plays an important role in the processes described in this study, is determined by the model. These adjustments are a drawback if ECHO-G is compared to other simulations that do not use flux corrections (e.g. Vellinga and Wu 2004; Jungclaus et al. 2005) since their need is an indication of erroneous feedbacks in the transient climate (Marotzke and Stone 1995). The degree to which they may affect the results shown herein is not known. However, large impacts are not expected since the mechanisms that will be described are comparable in physics and time scales to those of other simulations without flux corrections.

The study makes use of five different simulations: a 1000-year control simulation (CTRL), two forced simulations for the period 1000–1990 AD (FOR1 and FOR2), and two future scenario simulations (A2 and B2) that extend FOR1 until 2100 AD. In CTRL the external forcing is fixed to present day values ($[\text{CO}_2] = 353 \text{ ppm}$; $[\text{CH}_4] = 1,720 \text{ ppb}$; $[\text{N}_2\text{O}] = 310 \text{ ppb}$; solar constant = 1.365 W m^{-2}). The forced simulations of the past millennium (FOR1, FOR2) use identical estimates of natural and anthropogenic forcing factors: solar irradiance, the radiative effects of stratospheric volcanic aerosols, and concentrations of greenhouse gases (CO_2 , CH_4 and N_2O) based

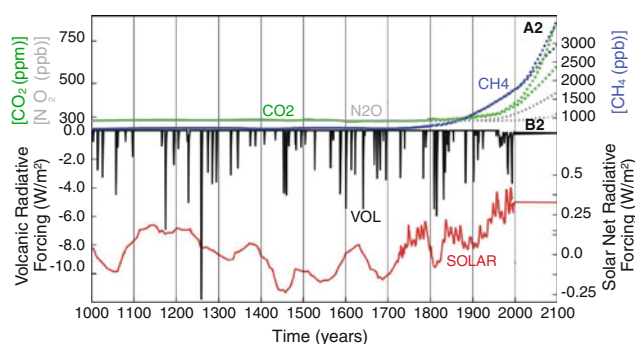


Fig. 1 Estimations of natural and anthropogenic forcing factors used to drive the ECHO-G model: solar irradiance (red line), greenhouse gas concentrations (green, grey and blue lines for CO₂, N₂O and CH₄, respectively), and the radiative effect of volcanic aerosols (black lines). Figure modified from González-Rouco et al. (2009)

on reconstructions provided by Crowley (2000). Figure 1 shows the time evolution of all these forcing factors. In particular, the representation of the volcanic forcing is rather simplified, with the effect of volcanic aerosols incorporated as global variations in the effective solar constant. Note that changes in tropospheric sulphate aerosols and vegetation, both of which are likely to attenuate the warming trends in the twentieth and twenty-first centuries (Bauer et al. 2003; Osborn et al. 2006) are not included. Within the climate change scenarios net solar irradiance is kept constant and fixed to the value of year 1990, and GHG concentrations vary according to the IPCC emission scenarios A2 and B2 (Nakicenovic et al. 2000).

The two long forced simulations start from different initial conditions. FOR1 is initiated from year 17 in CTRL and FOR2 from year 1700 AD in FOR1. In both cases a spin down period of 100 years was allowed to drive the model to equilibrium with the forcing conditions of year 1000 AD. The initial state was comparatively warm in FOR1 and the spin down period proved to be too short to reach at least equilibrium in surface temperatures (Goosse et al. 2005; Osborn et al. 2006). In turn, FOR2 was started from a colder state and its temperature variability was found to be well within the range of other millennial simulations (Jansen et al. 2007; Zorita et al. 2007). Both FOR1, and to a lesser degree, FOR2, exhibit initial trends in the deep ocean, indicating that it requires some time to reach thermal adjustment. For that reason, the first two centuries of each simulation, which incorporate the largest drifts, will not be considered in this study. In the analysis that follows, it will become apparent that the differences introduced by the initial conditions have a small impact on the climatology and the main mechanisms described.

A more detailed description of the model setup, the forcing and the simulations can be found in Zorita et al. (2004) and González-Rouco et al. (2009). Internal climate

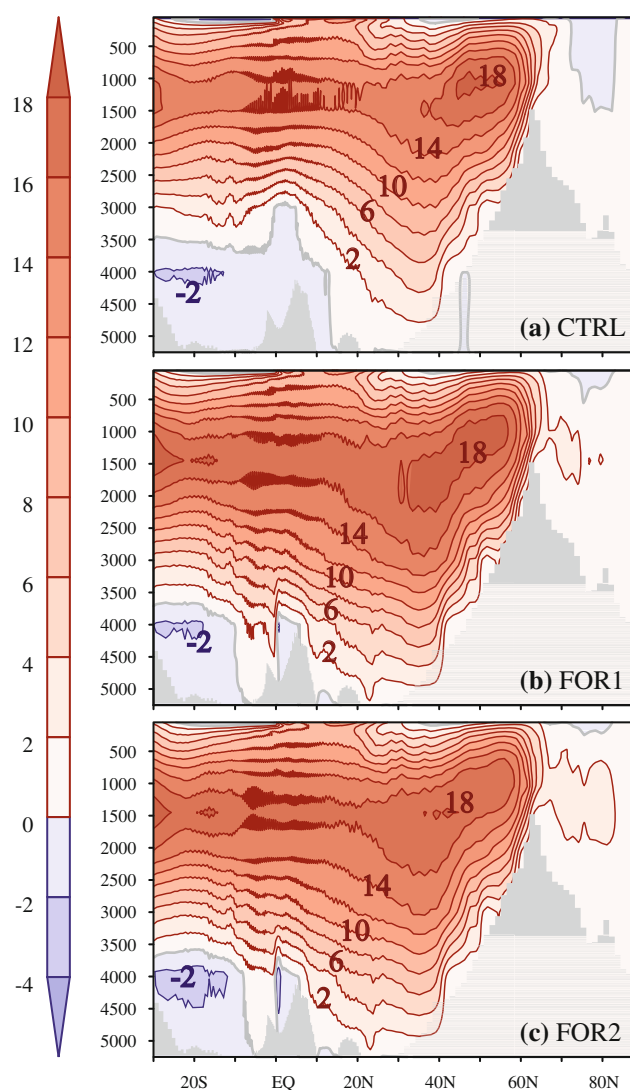


Fig. 2 Mean of the AMOC streamfunction (in Sv) for **a** CTRL, **b** FOR1 and **c** FOR2. Positive values of the streamfunction indicate clockwise circulation. Contour interval is 2 Sv

variability has been validated against instrumental data in the control run (Min et al. 2005a, b). Many features of the long forced simulations employed in our study have been analysed in previous works (González-Rouco et al. 2003a, b, 2006, 2009; von Storch et al. 2004; Zorita et al. 2003, 2005; Beltrami et al. 2006; Gouirand et al. 2007a, b; Stevens et al. 2007).

3 Climatology and temporal evolution of the AMOC

3.1 The mean AMOC state

Figure 2 shows the mean of the AMOC streamfunction for the three long simulations (CTRL, FOR1 and FOR2). All experiments exhibit a realistic circulation, with maximum

mean values comparable to North Atlantic Deep Water (NADW) estimates of 15 ± 2 Sv (Ganachaud and Wunsch 2000). The simulated Antarctic Bottom Water (AABW) inflow into the Atlantic is in all cases below estimates of 5–8 Sv (Orsi et al. 1999; Ganachaud and Wunsch 2000; Talley et al. 2003). Also, the NADW cell is generally deeper than indicated by recent observations (Talley et al. 2003) and other model climatologies (e.g. Dong and Sutton 2005; Mignot and Frankignoul 2005).

Deep water formation north of the Greenland-Scotland ridge (GSR) is negligible in CTRL, and accounts for a GSR overflow of 2–3 Sv in FOR1 and FOR2. Yet, its strength is underestimated if compared to observations (6 Sv; Hansen and Østerhus 2000; Olsen et al. 2008). The discrepancy among simulations points to differences in the properties of water masses in the North Atlantic. Indeed, the reservoir north of the sills is climatologically lighter in CTRL, both due to fresher and warmer waters, exhibiting also less convective activity (not shown). Similar conditions are also observed in the scenario simulations (A2 and B2) and will be detailed in Sect. 6.3 In contrast, in the forced experiments the overflow brings dense waters to the subpolar North Atlantic, contributing to a stronger AMOC below 1,500 m.

3.2 Variability of the AMOC strength

The meridional overturning index (MOI), first defined by Delworth et al. (1993) as the maximum value attained by the Atlantic meridional overturning streamfunction, is often employed to characterise the AMOC strength, since it is both intuitive and robust against changes in models and simulations (e.g. Delworth et al. 1993; Weaver and Valcke 1998; Timmermann et al. 1998; Delworth and Greatbatch 2000; Thorpe et al. 2001; Delworth et al. 2002; Gregory et al. 2005; Mignot and Frankignoul 2005). In order to focus on decadal to multidecadal variability, Fig. 3 shows the temporal evolution of a 11-year running mean of the MOI in the five ECHO-G simulations. In broad terms, AMOC variations in FOR1 and FOR2 are within the range of variability in CTRL. Besides, FOR1 tends to exhibit larger values than FOR2, as a result of their different initial stratification, given that all other factors are the same (Sect. 2) A common feature to both simulations is a weakening of the AMOC beginning with the industrial era that continues along the scenario simulations (Fig. 3). By the last decade of the twenty-first century, the MOI experiences a decrease of 35% in B2, and 42% in A2 relative to the mean preindustrial value in FOR1 (ca. 20 Sv). We will show in Sect. 6.3 that this decrease is mainly caused by increased precipitation at high latitudes. The larger decrease in A2 seems reasonable, since this scenario is characterised by stronger emissions. This future response is

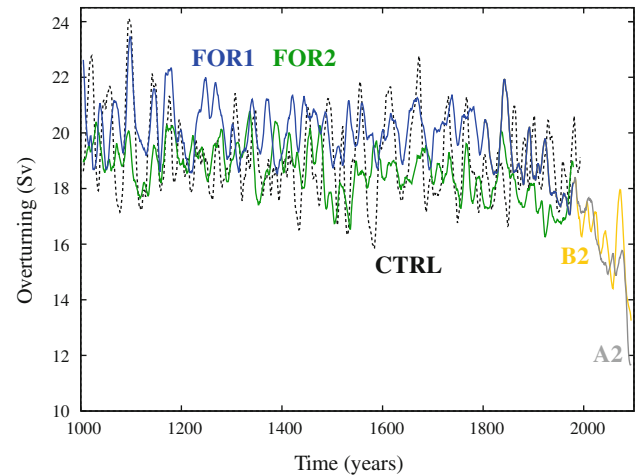


Fig. 3 Time series of the MOI (in Sv) in the Atlantic for CTRL (black dashed line), FOR1 (blue line), FOR2 (green line), A2 (grey line) and B2 (yellow line). The series are smoothed with an 11 year running-mean filter

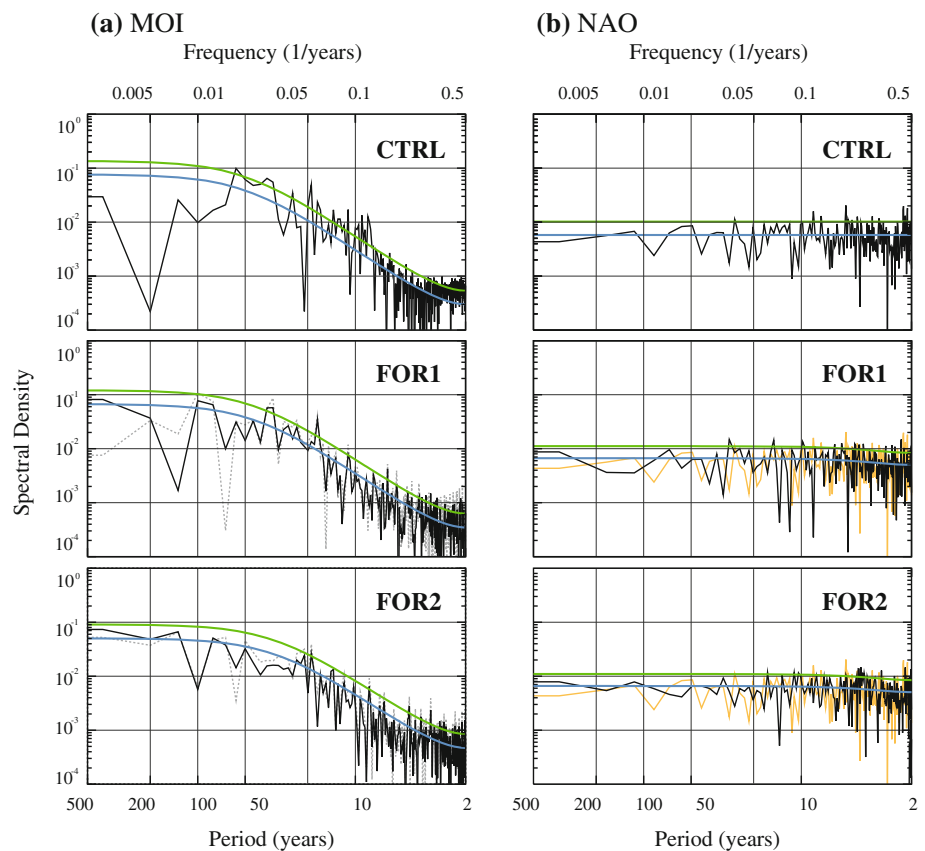
most probably overestimated due to the lack of sulfate aerosols (Delworth and Dixon 2006) in all the simulations.

Fourier spectra of the unfiltered MOI (Fig. 4a) indicate that the AMOC behaviour is approximately described by a red-noise process in all three millennial simulations (note that the scenarios are excluded). Variance exceeds slightly that of a first order autoregressive process (AR1) at inter-annual and interdecadal time scales, suggesting that other processes than just the integration of synoptic weather noise by the ocean (Hasselmann 1976) contribute to variability at these time scales. The peaks of variance are most clear in CTRL, and less so in the forced runs (particularly at interdecadal timescales). The analysis of AMOC variability at both frequency ranges will be addressed separately in Sects. 4 and 5. Finally, in the lowest frequencies (periods above 100 year) the CTRL run presents relatively small spectral densities as compared to the forced runs, and also to its corresponding AR1 process. The larger values in FOR1 and FOR2 are possibly an indicator of some modulation from the external forcing at centennial timescales. This increased low-frequency MOI variability is partly explained by the AMOC weakening trend in the period 1800–1990, that accounts respectively for 29 and 8% of the total industrial variance in FOR1 and FOR2. Indeed, if the industrial period is excluded, spectral values in both simulations exhibit a general decrease at periods above 50 years (dotted grey lines in Fig. 4a).

3.3 Analysis of the maximum AMOC location

As indicated by Vellinga and Wu (2004) and Dong and Sutton (2005), the location at which the AMOC maximum is found varies with time, thus hindering the physical

Fig. 4 Fourier spectrum of: **a** the MOI and **b** the NAO series in the millennial simulations CTRL (*top*), FOR1 (*middle*) and FOR2 (*bottom*). The *black solid lines* represent the spectrum calculated for the complete simulations. In the forced runs, the *grey dotted lines* correspond to the spectrum in the preindustrial period (1000–1800). In the *right panel*, the *orange lines* reproduce the spectral values for CTRL, to ease the comparison with those of the forced runs. The *blue lines* represent the spectrum of a red-noise process with the same first autoregressive coefficient as the complete time-series. The *green line* sets the 90% confidence interval of this red-noise process



interpretation of the MOI variability. In order to assess the robustness of the MOI, the variability in the location of the maximum streamfunction value in terms of latitude and depth is analysed (Fig. 5; results are shown only for A2 since those obtained for B2 are qualitatively very similar). In CTRL the location of the maximum is quite stable, oscillating in a small band of latitudes around 50°N and mainly confined to the 1,050 m depth. Indeed, about one third of the time the temporal maximum occurs at the same location as the long-term mean maximum (47.4°N and 1,050 m). In contrast, the forced experiments are characterised by the location of the AMOC maximum varying in a wider range of latitudes as well as depths. This suggests that the external forcing has a clear impact on the position of the maximum, even if both the latitude and depth at which the maxima occur are uncorrelated with the different forcing factors (not shown). Indeed, the position of the maximum exhibits some low-frequency modulation in the forced runs, not so clear in CTRL. In both forced runs the maxima are found between 10°N and 56°N, while these are concentrated in a narrower latitudinal band in CTRL. Also, FOR2 seems to exhibit some more latitudinal variability than FOR1. During the first centuries of FOR1 the maximum is more confined to latitudes from 36°N to 56°N, and only around 1800 AD this range seems to broaden. The

main discrepancies between FOR1 and FOR2 are observed in depth. In FOR1, the maximum starts varying in a broad range of levels, from 1,000 to 2,100 m. These variations are shallower in FOR2, probably due to its different initial conditions. Indeed, FOR2 was started from year 1700 AD in FOR1, a period when the position of the maximum starts to become shallower, and varies at similar depths as in FOR2. This shoaling of the maximum continues through the last three centuries of FOR1, and becomes more important during the scenario simulations. In either case, both forced and unforced simulations exhibit changes in depth and latitude that seem to be correlated, with maxima located at lower (higher) latitudes more likely to occur at deeper (shallower) levels. This suggestion is supported by linear correlations between both quantities of -0.57 , -0.67 and -0.74 for CTRL, FOR1+A2 and FOR2, respectively.

Since the MOI is calculated as a maximum value, with its position varying in a wide region of the North Atlantic (Fig. 5), its short-term variability averages the signal across different locations, thus hampering the identification of the possible mechanisms operating at smaller spatial scales (see Sect. 4). This limitation of the MOI has led some authors to consider alternative overturning indices. Vellinga and Wu (2004) fixed the latitude near the climatological maximum of the AMOC streamfunction to obtain a

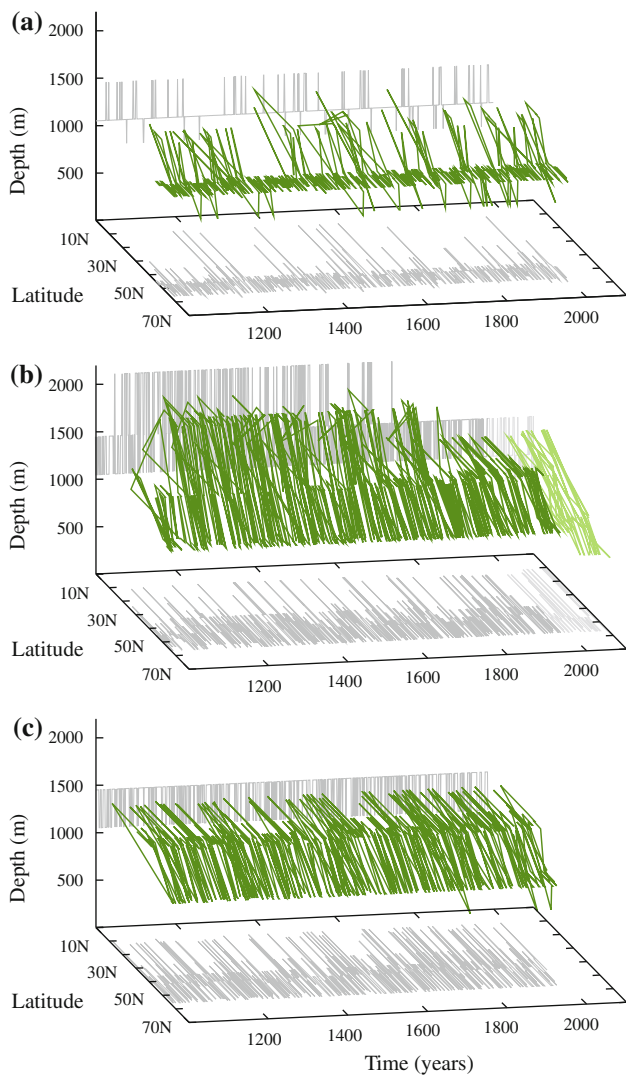


Fig. 5 Evolution of the position of the AMOC maximum in the simulations: **a** CTRL, **b** FOR1+A2, **c** FOR2. The *green line* describes in a three-dimensional plot the temporal variability of the location where the maximum AMOC takes place. The *light grey lines* represent the projections of the green line on the time-latitude and time-depth planes. *Light colors* in **b** correspond to the evolution during the scenario simulation

better representation of variability at interannual time scales. Similar definitions, with the overturning strength evaluated at fixed locations, have also been used in an attempt to link the AMOC variability to specific processes in the North Atlantic, such as convection in the Labrador Sea or NAO variability (Eden and Jung 2001; Eden and Willebrand 2001; Eden and Greatbatch 2003) or to gauge its variability at the latitude of the RAPID ocean observation array (e.g. Baehr et al. 2008). Finally, another alternative is the use of EOF/PC analysis (e.g. Vellinga and Wu 2004; Msadek and Frankignoul 2009).

In the following, Sects. 4 and 5 will address separately the high and low frequency variability in the AMOC. To

analyse the high-frequency several local indices will be introduced in order to survey the different AMOC responses in the North Atlantic and identify the mechanisms responsible for these variations. In this way the diverseness of the local overturning short-term variability is better represented. The selection will be made within the locations where the AMOC streamfunction maxima have been found to take place in the simulations (Fig. 5).

4 Mechanism of high-frequency AMOC variability

The main goal of the following two sections is to identify which mechanisms drive the AMOC variability in the ECHO-G model at high (i.e. interannual) and low (i.e. decadal to centennial) frequencies. Previous studies (Eden and Willebrand 2001; Vellinga and Wu 2004; Mignot and Frankignoul 2005; Cabanes et al. 2008) suggest that surface atmospheric circulation dominates the AMOC inter-annual variability through changes in Ekman transport. Variance exceeding that of a red noise process in the shorter timescales (2–5 years) of the Fourier spectra (Fig. 4a) also suggest a role of the atmospheric forcing. Such atmospheric forcing at high-frequencies would explain the fast variations observed in the location of the maximum (Fig. 5). Thus, a correlation analysis between both the global atmospheric fields of sea level pressure (SLP) and wind stress, and a set of local overturning indices is performed. In order to sample the regions where the AMOC becomes more intense, only those locations where the AMOC streamfunction reaches a maximum value (Fig. 5) were considered. The local AMOC time-series at these sites (ranging in number from 24 in CTRL to 22 in FOR2 and 30 in FOR1) were selected and high-pass filtered by removing variability at time scales longer than 10 year. The filter employed uses least squares coefficients to reduce Gibbs oscillations (Bloomfield 1976) and is characterised by a sharp transfer window that allows an accurate selection of the different timescales.

Inspection of the correlation maps between the aforementioned surface atmospheric fields and the AMOC indices suggests the local series can be classified into four categories represented by the indices at only four locations (Table 1; note that the indices MOI-loc1 to MOI-loc4 are ordered by decreasing latitude). Their associated atmospheric patterns are shown in Fig. 6. Correlations with the MOI (Fig. 6, last row) generally exhibit a weaker signal than those with locally defined indices. This result is to be expected due to the integration by the MOI of different local influences across the North Atlantic basin. Here, as in the remainder of the text, statistical significance of all the regression/correlation coefficients is assessed following a Student's *t* test. The sample size is corrected by taking into

account the series autocorrelation, thus reducing the sample degrees of freedom to its effective value (Bretherton et al. 1999). Correlation values are maximum at lag 0, and drop substantially at other lags (not shown), thus showing evidence of a fast overturning response to the atmospheric forcing at high-frequencies.

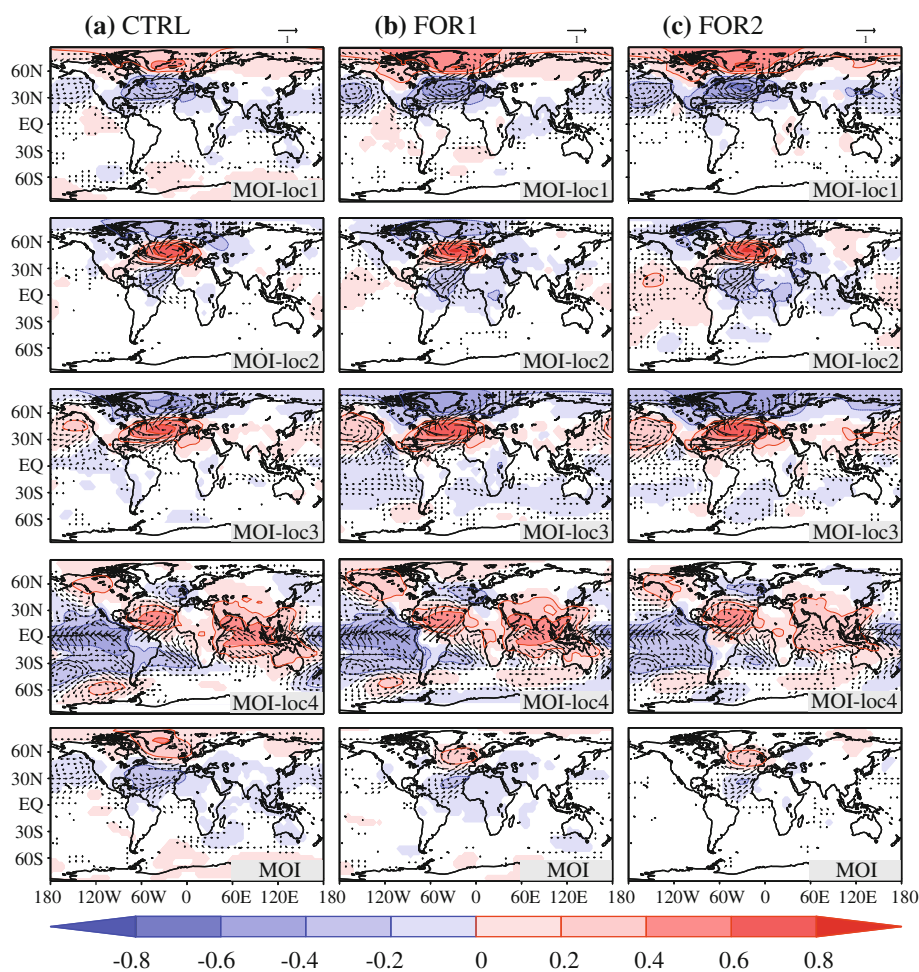
The opposing phases of a zonally extended NAO-like SLP pattern (e.g. Wallace and Gutzler 1981) are identified for both MOI-loc1 and MOI-loc3. At mid-latitudes, represented by MOI-loc2, the overturning variability is linked to an intense anticyclonic cell centred north of the Azores islands (around 55°N and 30°W) that introduces a west-east gradient over western Europe, and is accompanied to the south by a band of negative pressure anomalies. These are the main features described for the negative phase of

the East Atlantic (EA) Pattern by Barnston and Livezey (1987). The negative anomalies across Greenland and the Nordic Seas, as opposed to the positive cell at midlatitudes, indicate that some weak contribution from the NAO may also be present. MOI-loc4 is the only index defined at tropical latitudes and is associated with a large-scale pressure pattern with a noticeable signal in the tropical Pacific, that is likely evidencing the influence of ENSO variability (e.g. Trenberth and Shea 1987). The model's performance to reproduce both ENSO and NAO variability has been previously analysed in CTRL (Min et al. 2005b). Overall, both indices are well represented as compared to observations and other model simulations. The occurrence of ENSO is however too frequent, and its amplitude too large. The main NAO bias is an overestimation of its impact over the Pacific sector. Likewise, the centers of action of the EA pattern (Fig. 6, second row) are in general good agreement with those observed in other models (e.g. Fig. 3b in Msadek and Frankignoul 2009). Linear correlations (Table 2) support the observed links between the MOI-loc4 and ENSO, between the NAO and both MOI-loc1 and MOI-loc3, and also between MOI-loc2 and the

Table 1 Position of the local overturning indices used in Sect. 4

	MOI-loc1	MOI-loc2	MOI-loc3	MOI-loc4
Latitude (°N)	55.8	41.8	33.5	10.0
Depth (m)	1,050	1,450	2,100	1,450

Fig. 6 Correlation maps of the local overturning indices (see Table 1) with SLP (*shaded*) and wind stress (*vectors*) anomalies. Data have been high-pass filtered for time scales below 10 year. All correlation values are significant at a 0.05 level according to a Student's *t* test and accounting for the effective sample size by considering autocorrelation



EA timeseries. In addition, all simulations show weaker but significant contributions from the NAO to MOI-loc2 variability, as well as from the EA to the MOI-loc4. Interestingly, all local indices show similar correlation patterns in the three millennial experiments, and also similar correlations with the main teleconnection indices. For the sake of brevity, the analysis in high-frequencies will continue focused exclusively on the CTRL run, with results for the other runs leading to similar conclusions.

The underlying mechanism for the overturning response to the former teleconnection patterns (i.e. NAO, ENSO and EA) is now explored (Fig. 7). The large-scale patterns modulate the zonal wind at different latitudes, thereby inducing local changes in the meridional Ekman transport. Figure 7 shows the spatial extension of AMOC changes (bottom panels) in the context of the zonal wind variations (top panels) associated with each teleconnection index. Note that, in the Northern Hemisphere, easterlies force northward and westerlies southward meridional transport, while transports are reversed in the Southern Hemisphere. In broad terms, the surface wind forcing is found to generate deep, latitudinally narrow and relatively local overturning cells. In the case of the NAO (Fig. 7a), easterlies around 30°N force surface transport to the north, while westerlies near 50°N force southward transport. Convergence of water masses at 43°N results in local downwelling, thus originating two overturning cells of opposite sign. This is consistent with the fact that MOI-loc1 and MOI-loc3 lie in the regions with largest negative and positive anomalies, respectively. This pattern with opposing cells and downwelling near 40°N resembles the instantaneous ocean response to the NAO first described by Eden and Willebrand (2001) and also found in later studies (Vellinga and Wu 2004; Mignot and Frankignoul 2005; Deshayes and Frankignoul 2008). The pattern associated

with ENSO (Fig. 7b) is characterised by a large overturning cell confined to the tropical Atlantic, consistent with the first EOF obtained by Vellinga and Wu (2004) at interannual time scales, which they also relate to El-Niño variability. In this case, the overturning cell is wider in latitude, as a response to the combined effect of westerlies to the south and easterlies to the north of the Equator, both forcing northward meridional mass transport. Obviously,

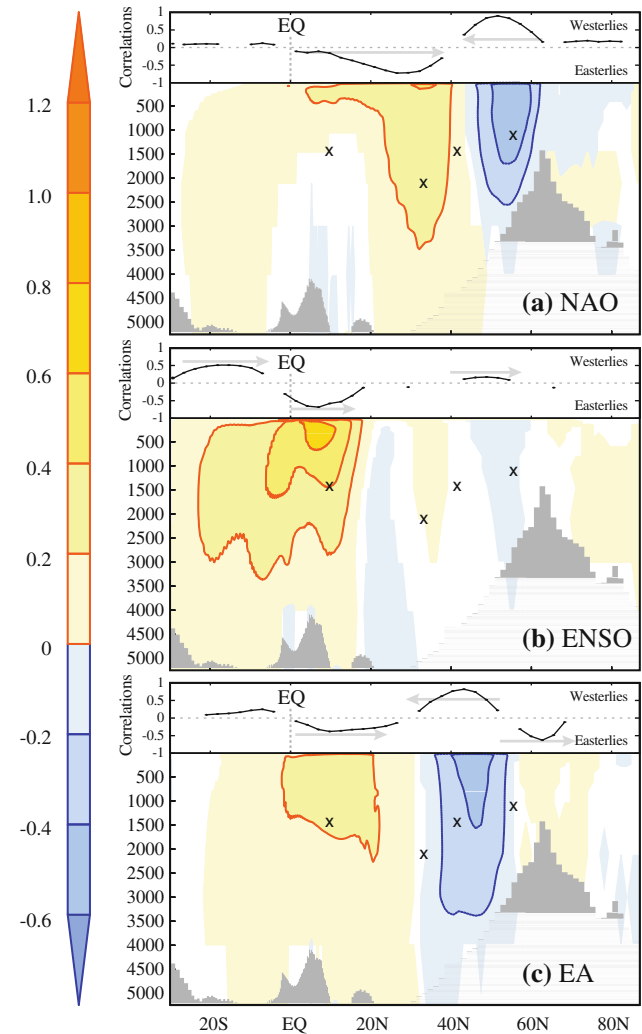


Table 2 Correlations between the high-pass filtered (periods ≤ 10 year) local overturning indices and the indices of the main teleconnection patterns (see also Fig. 6)

		MOI-loc1	MOI-loc2	MOI-loc3	MOI-loc4
ENSO	CTRL	-0.06	0.01	0.07	0.49
	FOR1	-0.04	-0.02	0.09	0.49
	FOR2	-0.01	-0.11	0.02	0.38
NAO	CTRL	-0.42	0.16	0.51	0.05
	FOR1	-0.64	0.15	0.64	-0.04
	FOR2	-0.65	0.11	0.68	0.07
EA	CTRL	-0.04	-0.58	-0.06	0.25
	FOR	0.03	-0.64	-0.01	0.30
	FOR2	-0.10	-0.59	0.08	0.27

Values in bold represent correlations significant at the 0.05 level according to a Student's *t* test that takes into account the series autocorrelation to calculate the sample size

Fig. 7 Analysis of high-frequency wind-driven changes of the AMOC in CTRL. *Upper panels* correlation values between the zonally averaged zonal wind-stress and the timeseries of the main teleconnection patterns: **a** NAO defined as the difference between normalised SLP anomalies at the closest gridpoints to Azores and Iceland, **b** ENSO calculated as the 1st Principal component (PC) of SST in the tropical Pacific, **c** EA computed as the 3rd PC of SLP in the North Atlantic. *Arrows* indicate the direction in which the meridional Ekman-transport is produced. *Lower panels* regression maps between the AMOC streamfunction anomalies (in Sv), and the indices of the respective teleconnection patterns. The *crosses* mark the location where the local overturning indices are defined (note that MOI-loc1 to MOI-loc4 are ordered by decreasing latitude). Data filtering and significance is considered as in Fig. 6

only the index defined in the Tropics (MOI-loc4) is well placed inside the resulting overturning cell. Finally, and similarly to the NAO, the EA pattern is also linked to a dipole of narrow overturning cells (Fig. 7c), but more displaced to the south than those in Fig. 7a, given the influence of zonal winds further south. The regions with the largest positive and negative overturning anomalies map over the locations where MOI-loc4 and MOI-loc2 were defined, as expected after correlations in Table 2.

Our results confirm the influence of local atmospheric circulation on the AMOC interannual variability. The fact that the results are common in CTRL and the forced runs (Fig. 6, Table 2) furthermore suggests that at high frequencies changes in external forcing factors have no clear influence on the AMOC variability. In the next section the prominent features of the AMOC variability on longer time scales are explored.

5 Low-frequency AMOC variability

This section focuses on complementary timescales to those considered in Sect. 4, i.e. periods above 10 years. At low frequencies, the MOI is related at lag 0 to overturning variability over the whole Atlantic basin for each of the long simulations (Fig. 8, middle panels). Although the highest regression coefficients are found in the NADW formation region, common basin-scale variability is found from the North Atlantic to the Equator, indicating that at these timescales the MOI gauges the variability of the entire AMOC cell.

The development of these basin-scale anomalies begins in the NADW formation region (Fig. 8, top panels), and takes place gradually over several years, attaining its maximum values at lag 0. Indeed, the low-pass filtered MOI is significantly autocorrelated for lags up to 5–8 years (Fig. 8, bottom panels). These autocorrelations are also significant for the unfiltered index (not shown), thus supporting a predominant AMOC mode at interdecadal timescales. Similar slowly-developing MOC variations have been observed in the context of some ocean oscillatory modes in other models (e.g. Timmermann et al. 1998; Dong and Sutton 2005; Hawkins and Sutton 2007). In the ECHO-G simulations, a thorough understanding of this AMOC mode would require a complete description of the mechanisms and cycles involved that is beyond the scope of this study. In the following, a first insight on the mechanisms behind the AMOC strengthenings is given instead.

At the low-frequencies, most of the mechanisms described (e.g. Timmermann et al. 1998; Dong and Sutton 2005; Mignot and Frankignoul 2005; Hawkins and Sutton 2007) relate the AMOC variations to changes in North Atlantic deep convection. Thus, in order to investigate the

mechanism responsible for interdecadal AMOC variability, the link between the MOI and the variability of the mixed layer depth (MLD) in the long simulations is explored (Fig. 9, left column). The analysis shows that positive MOI variations are preceded by increased activity south of Greenland, with maximum correlation coefficients for a leading time of 4 years. Likewise, recent analyses with both observations and regional modelling (Bacon et al. 2003; Moore 2003; Pickart et al. 2003) suggest that deep convection events in the Irminger Sea may be forced by a so-called Greenland tip jet that enhances heat loss through both fairly localised air-sea heat flux and strong wind-stress curl. A similar mechanism seems to be taking place in the ECHO-G simulations, in spite of the relatively coarse resolution of this model. Indeed, the correlation maps in Fig. 9 (right column) show that increased convection is taking place in a context of negative winter SLP anomalies over Greenland, along with intensified westerlies from the Labrador to the Irminger Seas, and increased wind-stress curl southeast of Cape Farewell. This general picture is also compatible with the ocean response to NAO variability described by Deshayes and Frankignoul (2008), in which the NAO was found to drive Irminger convection through anomalous Ekman pumping over the region.

To identify the precursors for deep water formation the rest of the analysis is performed focusing on convection south of Greenland. Figure 10 shows lead-lag cross-correlations between the mean mixed layer depth anomalies in the convection regions near Cape Farewell (grey box in Fig. 9) and the averages of other variables in the same region. The MOI is found to lag the changes in convection by 4 years (dashed line in Fig. 10) in consistency with Fig. 9. The possible role of different quantities to foster convection is now explored (Fig. 10). No leading contribution on convection is found for either the averages of heat and freshwater fluxes (both precipitation and evaporation), the surface atmospheric temperature, or the mean ocean temperature and salinity values at different depths (not shown). Most interestingly, variations of the zonal wind-stress do precede by about 1 year the changes in convection.

Hence, the atmosphere appears, again, as the main source of low-frequency changes in convection, which leads in turn the AMOC changes. In the forced runs, these atmospheric variations seem to be ultimately forced by the NAO, with a lead time of 1–2 years (grey dashed line in Fig. 10, right panels). In the CTRL run, the contribution of the NAO is not significant. To understand this different influence the spectral and spatial features of the NAO are investigated. A Fourier analysis of their respective time-series shows some enhanced low-frequency NAO variability in the forced runs with respect to CTRL (black and orange lines in Fig. 4b). Some differences are also observed in the NAO spatial configuration. The latitudinal

Fig. 8 *Top* Lag-regression maps between the low-pass filtered maximum overturning strength and the anomalies of the AMOC streamfunction (in Sv) in CTRL (*left*), FOR1 (*middle*) and FOR2 (*right*). Positive (negative) lags indicate that the streamfunction pattern lags (*leads*) the MOI timeseries. *Bottom* autocorrelation of the low-pass filtered MOI timeseries (periods above 10 year). The *horizontal dashed lines* delimit significance at the 0.05 level. In all panels significance is assessed as in Fig. 6

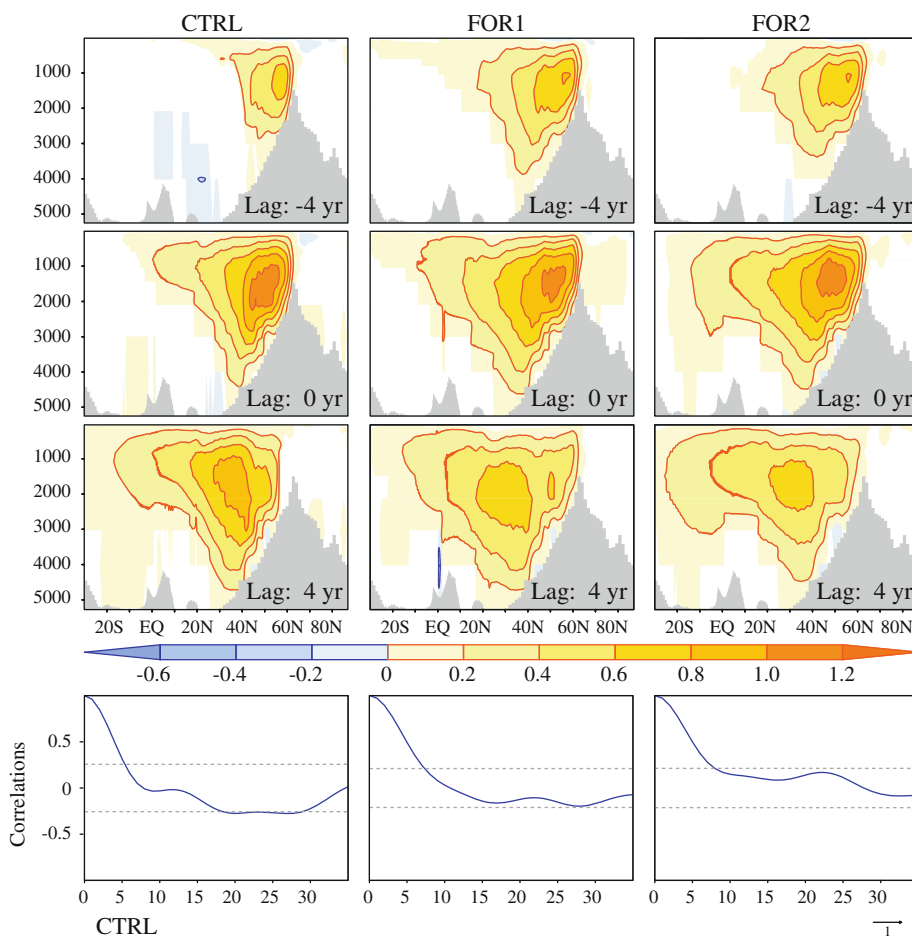


Fig. 9 Lag correlation maps between the MOI and: (*left*) the winter (January–February–March) anomalies of the mixed layer depth in the 3 long simulations; (*right*) the winter means of the wind stress (*vectors*), the wind stress curl (*shaded*) and the SLP anomalies (*contours*). Filtering and significance is considered as in Fig. 8. The lag-correlations are calculated with the MOI lagging by 4 years, since this lag is associated with the largest correlation coefficients. The *grey rectangle* encloses the region where variables in Fig. 10 are averaged. The *contour interval* for correlations with the SLP is 0.2

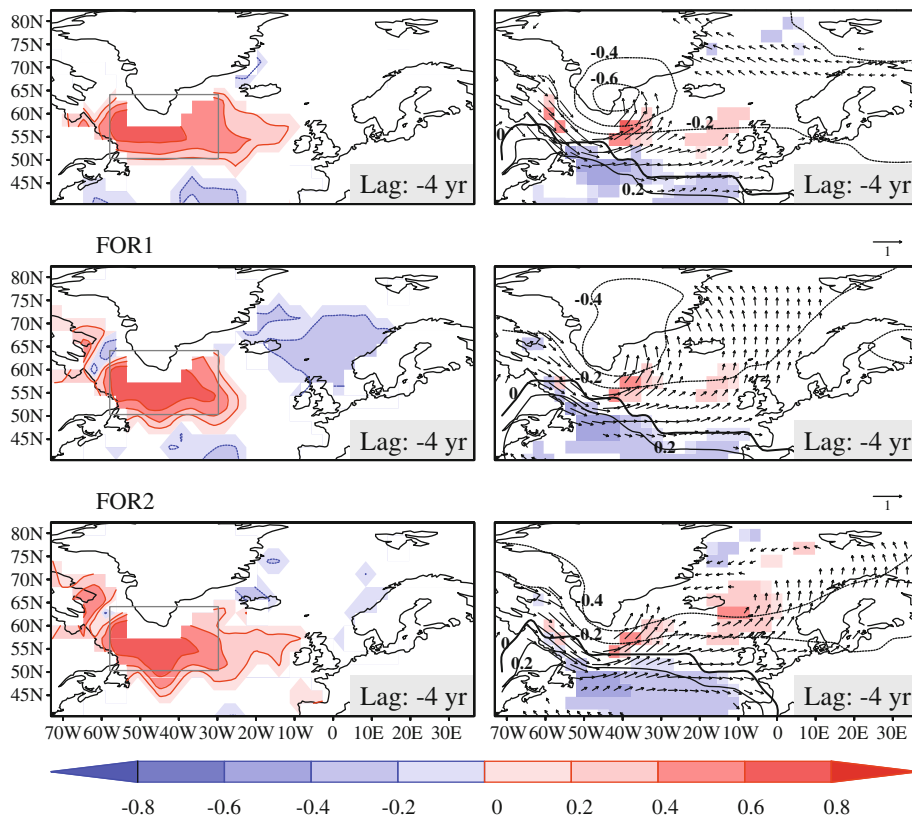
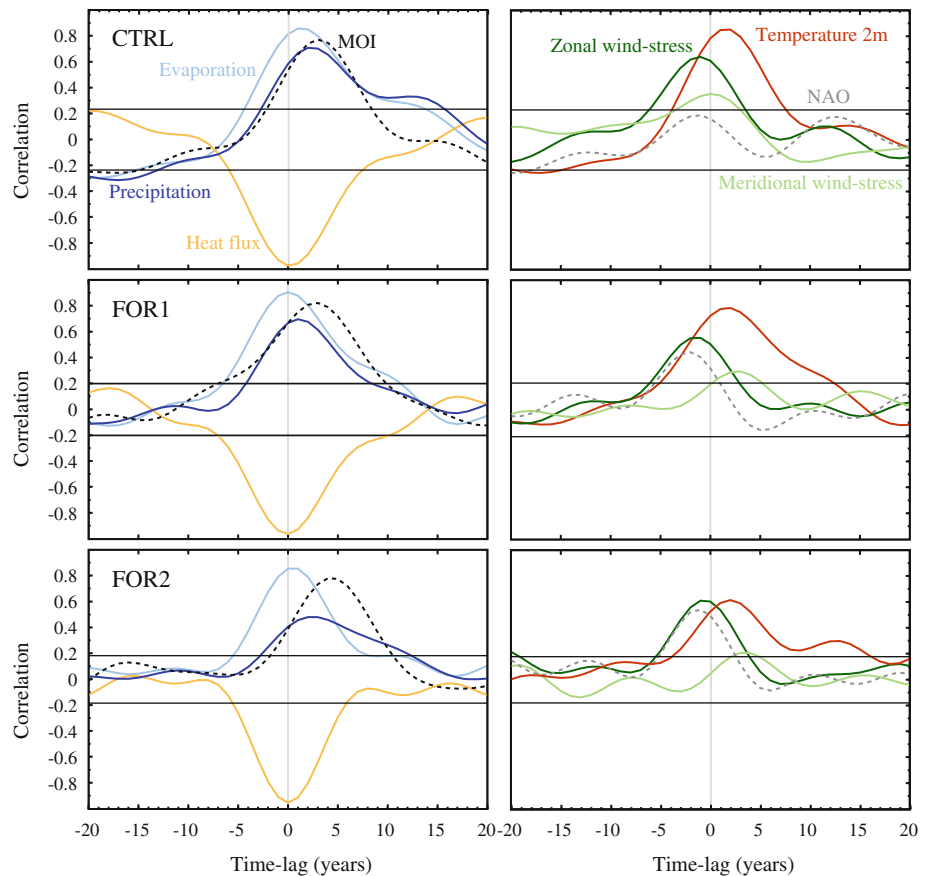


Fig. 10 Time-lag correlations between the average of mixed layer depth in the Labrador Sea (grey box in Fig. 9) and the averages of other variables in the same region. Correlation values with the main fluxes are shown on the *left side*, and with the main atmospheric variables on the *right*. Correlations with the MOI and the NAO timeseries (dotted black and grey lines, respectively) are also shown. The horizontal black lines delimit significance at the 0.05 level. Filtering and significance are considered as in Fig. 8. Positive (*negative*) lags indicate that convection is leading (lagging) the other variables



SLP gradient is stronger in the forced runs (Fig. 11), which also shows anomalous low pressures over Greenland. Both changes are accompanied by increased westerlies over the North Atlantic and intensified Greenland tip jet, which has been shown to drive Labrador convection, and thereby the AMOC. Other studies support the role of positive NAO phases to favour deep convection events in both the Labrador (Dickson et al. 1996; Guemas and Salas-Mélia 2008) and Irminger Seas (Pickart et al. 2003; Deshayes and Frankignoul 2008). These results suggest spatial SLP changes in FOR1 and FOR2 are being forced through the effect of the external forcing (both natural and anthropogenic) on tropical and subtropical SSTs, which can potentially impact the NAO (e.g. Rodwell et al. 1999; Peng et al. 2005). Given the impact of external forcing on atmospheric variability and the NAO in particular, and by extension its possible modulation of AMOC variability in FOR1 and FOR2, the following section investigates the specific AMOC response to each forcing factor.

6 Analysis of the AMOC response to the forcing

While most models predict a slowdown of the overturning strength in response to increasing GHG concentrations

(Schmittner et al. 2005; Schneider et al. 2007), the effect of the comparatively moderate radiative forcing (i.e. volcanic aerosols and solar irradiance) on the AMOC variability has received less attention and is less clear (e.g. Zorita et al. 2004; Stendel et al. 2006; Stenchikov et al. 2009; Swingedouw et al. 2010; Ottera et al. 2010).

A preliminary analysis, focusing on the preindustrial era to omit the predominant effect of greenhouse gases, is carried out in order to investigate the linear relationships between the natural forcing factors and the MOI. Neither the solar irradiance nor the radiative effect of volcanic aerosols are significantly correlated with the MOI, either at lag 0 (Table 3) or at other lead-lag times (not shown). Moreover, the effective solar constant, that accounts for the combined effect of both forcing factors, appears also unrelated to the changes in the MOI. The lack of a significant linear relationship between the AMOC strength and both the slowly changing radiative forcing and the fast-varying volcanic aerosols is also found by Hofer et al. (2011) for several transient simulations covering the last millennium. There is, however, an obvious need to improve the analysis, taking also into account the particularities of each forcing factor. The main changes of the AMOC and other ocean quantities related in response to each natural and anthropogenic

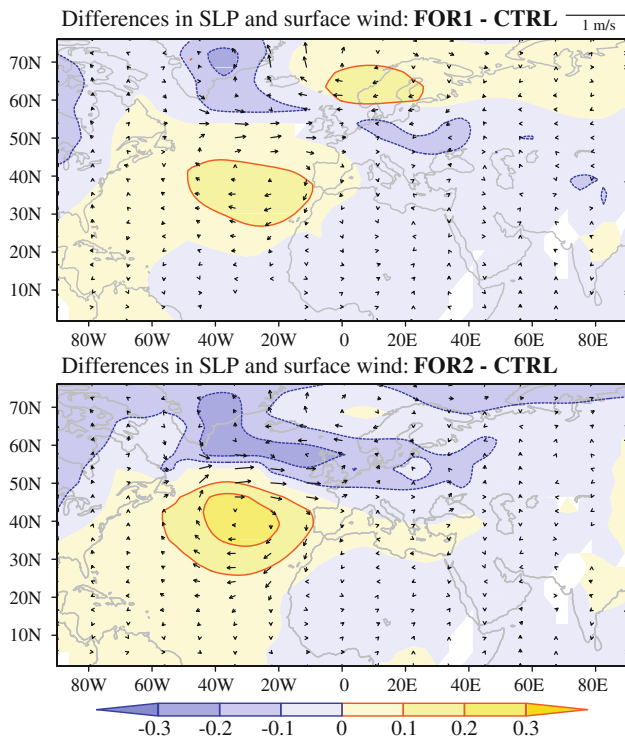


Fig. 11 Differences between the NAO regression patterns in the forced simulations and in CTRL. For each run, NAO is regressed with the anomalies of SLP (shaded, in hPa) and the surface wind (vectors, in m/s), and significance is assessed as in Fig. 6

Table 3 Correlations between the natural forcing and the MOI during the preindustrial period (1200–1850)

	Volcanic forc.	Solar forc.	Sol+Volc. forc.
FOR1	0.08	0.02	0.08
FOR2	-0.04	0.10	-0.01

Note that none of these values is significant at the 0.05 level according to a Student’s *t* test that takes into account the series autocorrelation to calculate the sample size

forcing factor are investigated separately in the following subsections.

6.1 Impact of solar irradiance

Studies addressing the impact of solar variability analyse the climate conditions during the Little Ice Age and, in particular, the Maunder Minimum (Rind et al. 2004; Zorita et al. 2004). These are periods characterised by a weak insolation (Fig. 1), but also remarkable volcanic activity. The actual role of the AMOC during this period remains unclear. Models often show little sensitivity to solar variability (e.g. Zorita et al. 2004; Stendel et al. 2006). Also, in some cases the AMOC is found to weaken in response to increased solar irradiance (Cubasch et al. 1997; Swingedouw et al. 2010) since North Atlantic convection is reduced due to the upper

ocean warming. In contrast, other studies (Sedláček and Mysak 2009a, b) report a wind-driven AMOC strengthening from the LIA to the present climate, favoured by a reduction of the sea-ice cover at high latitudes. There is more consensus regarding the main atmospheric conditions in the North Atlantic. Models show a general tendency to produce negative NAO phases during periods of low radiative forcing (Shindell et al. 2001; Rind et al. 2004; Zorita et al. 2004; Gouirand et al. 2007b; Swingedouw et al. 2010). In some of these studies NAO changes are found to lag the solar variations by 20 (Shindell et al. 2001) and 50 years (Swingedouw et al. 2010), triggered in each case via teleconnection mechanisms from the tropics and the Pacific ocean, respectively. Finally, NAO changes may have a subsequent impact on the ocean circulation. For example, Zorita et al. (2004) show that predominant low NAO phases lead to a weakening of the Gulf stream through a modulation of the wind-stress forcing (Zorita et al. 2004).

In the ECHO-G simulations, estimates of solar irradiance (Fig. 1) show a remarkable drop in solar activity from the Medieval Climate Anomaly (MCA; ca. AD 1100–1300) to the beginning of the LIA (ca. AD 1400–1600). Although both periods are also punctuated by the effect of volcanism, the main radiative difference can be assumed to be solar related. The significance of the AMOC changes associated with this decrease in total insolation is established by comparison with natural unforced variability. The AMOC change from the LIA to the MCA is studied by calculating the differences between the 200 year long periods defined above. Its significance is analysed by randomly extracting 1,000 comparable non-overlapping periods of 200 years in CTRL and calculating their respective differences. This provides a metric of the largest possible change related to solar forcing in the forced simulations compared to internal variability in CTRL. Only those values above the 97.5th or below the 2.5th percentiles are shown (Fig. 12a). Overall, the AMOC changes tend to be insignificant at the surface and also near the DWF region. The largest significant values are located at depth near the Equator, although with opposite sign in FOR1 and FOR2. At this location remarkable changes in both temperature and salinity are also observed (not shown). Since the deep ocean needs long time to reach thermal and haline adjustment, the different starting conditions in FOR1 (relatively warm) and FOR2 (relatively cold) can therefore explain the opposite AMOC changes in depth, pointing to too short a spin up period to achieve equilibrium at large depths. All these findings are difficult to reconcile with a meaningful solar impact on the AMOC.

The general ocean response to the solar forcing is also explored. To isolate the signal of solar variability, disregarding the contribution from volcanoes, the following study is based on different linear regressions with the

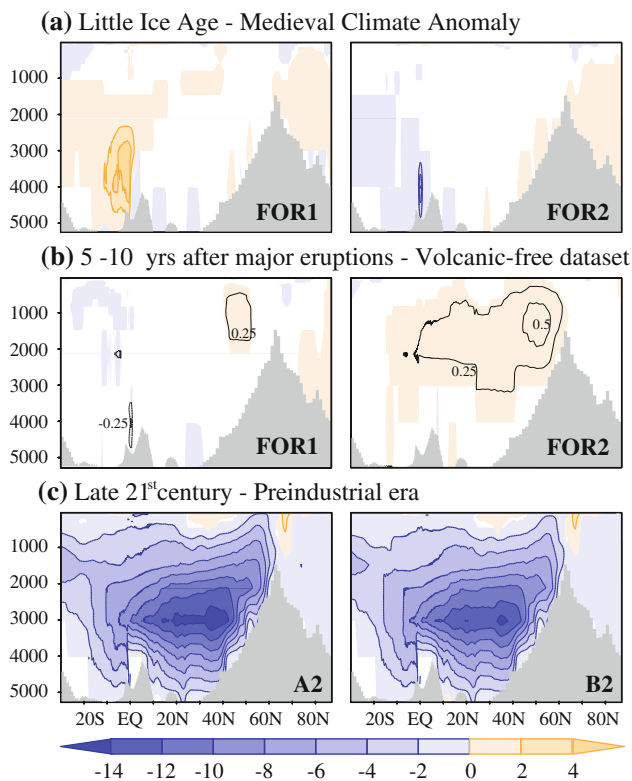


Fig. 12 Composites of the AMOC (in Sv) calculated as **a** the difference in means between the Little Ice Age (1400–1600) and the Medieval Climate Anomaly (1100–1300). **b** The average of preindustrial anomalies from years 5 to 10 after the 15 largest preindustrial eruptions. **c** The difference in means between the late twenty-first century (2070–2100) and the preindustrial era (1100–1850). Composites are shown for FOR1 (left) and FOR2 (right) in **a** and **b**, and for both A2 (left) and B2 (right) with respect to FOR1 in **c**. Black contours in **b** account for AMOC changes in increments of 0.25 Sv. Significance is assessed at the 0.05% level by comparing with the 2.5 and 97.5 percentiles in three different ensembles: **a** 1,000 pairs of non-overlapping 200 year long periods in CTRL, **b** 1,000 random selections of 15 years from a preindustrial volcanic-free dataset, **c** the 721 different 31 year long periods throughout the preindustrial era

standardised solar irradiance (Fig. 13). The sign of the solar index has been reversed to show results corresponding to a decrease in the solar activity (as occurred during the LIA). This new approach produces similar results for the AMOC to those in Fig. 12a (not shown). The reasons for the poor AMOC response to solar forcing are investigated through the analysis of other ocean quantities.

In both runs, surface salinity increases in the Arctic following an increase of the sea ice thickness that removes in turn fresh-water from the surface (Fig. 13a). However, the changes in salinity are rather weak and occur far from the Labrador and Irminger Seas, the region in the model that dominates deep water formation. The main response to the radiative cooling is observed for the SSTs (Fig. 13b), which shows a global pattern of negative anomalies, more intense in the Tropics. Yet, the anomalies in the vicinity of

the Labrador sea are also negligible. The most conspicuous disagreement between simulations is related to the atmospheric response (Fig. 13c). While FOR1 exhibits no significant changes, FOR2 shows a SLP pattern that has some resemblance to a negative phase of the NAO, introducing anomalous easterlies near Cape Farewell. However, the changes in wind-stress are not intense enough to affect Labrador and Irminger Sea convection, as becomes apparent in Fig. 13d. As a result, significant changes of winter convection are weak and mainly localised in the Norwegian Seas. This explains the little sensitivity of the AMOC to the solar variability, and in particular the fact that we find no response at the LIA. A similar picture arises for the ocean lagging the solar variations for up to 20 years (not shown).

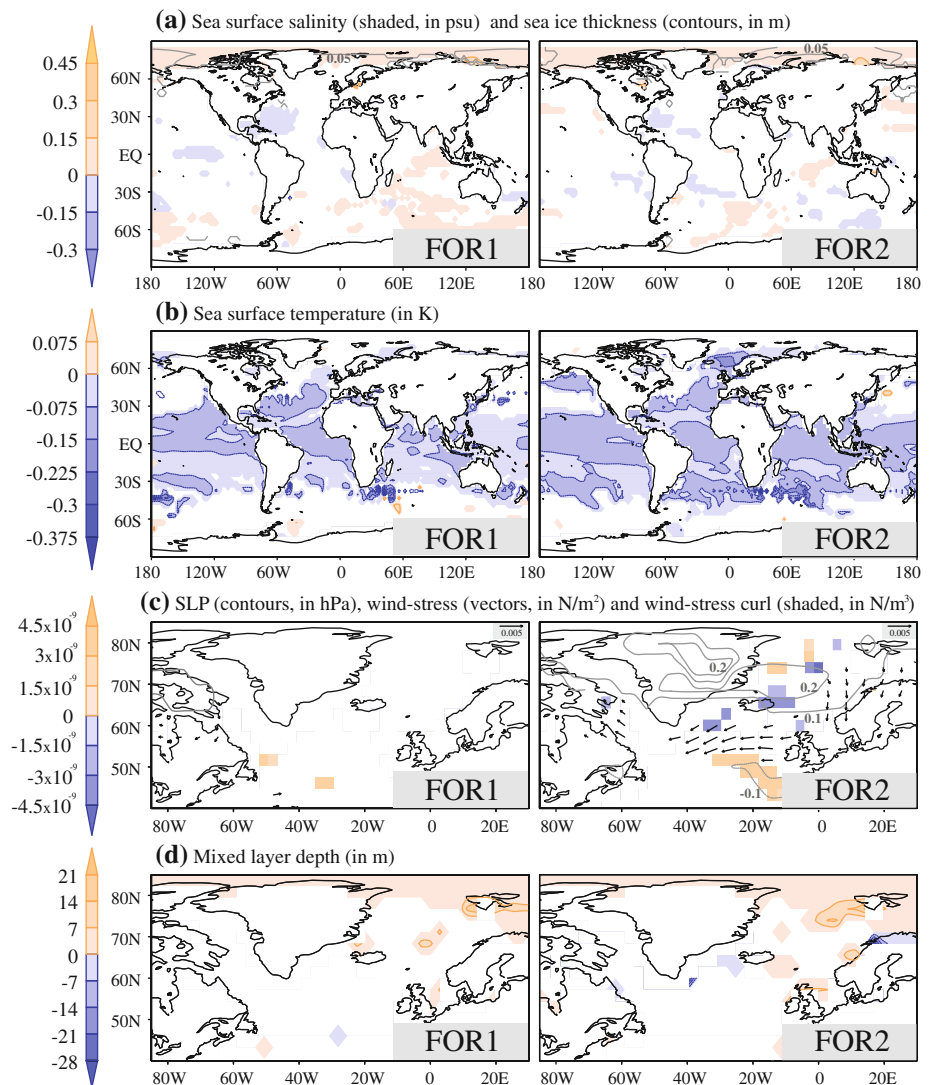
6.2 Influence from volcanoes

Unlike the solar irradiance changes, that range from decadal to multi-centennial timescales during the last millennium, volcanic aerosols have a relatively short-lived strong impact on the radiative forcing. The associated cooling signal can penetrate deep into the ocean, influencing the ocean thermal structure, and potentially producing low-frequency changes on global quantities, such as the ocean heat content, or the thermal expansion (Gleckler et al. 2006a, b). The particular ocean response to the 1815 Tambora and 1991 Pinatubo eruptions has been assessed by Stenchikov et al. (2009) using the GFDL model. Besides long-lasting changes in the ocean heat content and steric height, both major eruptions have been found to produce a 10% increase in the strength of the AMOC, triggered by enhanced convection favoured by denser conditions in the upper ocean. An overall AMOC increase is also observed in response to large tropical eruptions in the Bergen climate model (Ottera et al. 2010).

The non-linear episodic influence of volcanoes cannot be properly captured by the regression analysis applied to solar variability. Hence, a composite analysis is employed instead. The overall effect of volcanoes is characterised during the 15 largest preindustrial eruptions, their radiative forcing being at least half as large as for the 1815 AD Tambora eruption. To represent the periods without volcanic forcing, a volcanic-free dataset is defined that includes all the 237 years not preceded by a volcanic eruption in the previous decade. This latter choice is motivated by the fact that the analysis reveals that the volcanic fingerprint is almost negligible 10 years after the eruptions in both FOR1 and FOR2.

The composite maps in Figs. 12b and 14 are calculated as the average of preindustrial anomalies in the volcanic dataset, using a Monte Carlo test to assess significance. The reference Monte Carlo ensemble is computed by random

Fig. 13 Linear regression during the preindustrial period (1200–1850) between the negative and standardised index of solar irradiance and the following oceanic variables: **a** annual sea surface salinity (*shaded*, in psu) and winter sea ice thickness (*contours*, in m), **b** annual sea surface temperature (in K), **c** annual SLP (*contours*, in hPa), wind stress (*vectors*, in N/m^2) and wind stress curl (*shaded*, in N/m^3), **d** winter mixed layer depth (in m). Significance is assessed as in Fig. 6. The solar irradiance was reversed to show the patterns corresponding to a decrease of the solar activity



selection of 15 years from the volcanic-free dataset. 1000 different realizations are performed. As in the previous subsection, composite values are not significant if they fall within percentiles 2.5th and 97.5th of the ensemble. Figure 12b shows the averaged AMOC response from years 5 to 10 after the volcanic eruptions. Similarly to Stenichkov et al. (2009) and Ottera et al. (2010), and in contrast with the linear correlations in Table 3, a small but significant increase of the AMOC is found in the NADW formation region. Moreover, in the case of FOR2, positive streamfunction values up to 0.5 Sv are found all across the Atlantic basin. The analysis of other quantities help to understand how they develop.

The depth penetration of the volcanic signal is evaluated for temperature and salinity. Figure 14a shows that the cooling in the Atlantic ocean reaches down to 600 m in FOR1 and 1,000 m in FOR2, with the largest significant values in the upper 200 m. The impact on salinity is clearly

smaller, and mainly localised in the upper 50 m (Fig. 14b). In terms of latitude, the cooling is more important near the subtropics (Fig. 14c), with the most persistent negative anomalies occurring north of 55°N. North Atlantic convection is favoured by an increase in upper salinity that is partially due to a rise in sea ice thickness at high latitudes (Fig. 14d) and unrelated to changes in precipitation and evaporation (not shown). Both cooling and salinification contribute to denser conditions near the surface, thus leading to a slight increase in mixed layer depth both in the Nordic Seas (north of 63°N, Fig. 14e), and, to a lesser extent, in the Labrador and Irminger Seas (south of 63°N, Fig. 14e), which may explain the small strengthening of the AMOC (Fig. 12b). Unlike in Ottera et al. (2010), there is no significant NAO response to volcanoes (not shown), and therefore no wind-stress contribution to convection (vectors in Fig. 14e). This may explain the smaller AMOC changes in the ECHO-G model.

Fig. 14 Composites of the averaged preindustrial anomalies following the onset of the 15 largest preindustrial eruptions. The following variables are explored: **a** depth-dependent Atlantic mean temperature (in K), **b** depth-dependent Atlantic salinity (in psu), **c** Atlantic temperature in the upper 200 m (in K), **d** Atlantic salinity in the upper 50 m (shaded, in psu) and sea ice thickness (black contours, in m), **e** mixed layer depth (shaded, in m) and zonal wind-stress (vectors, in N/m^2). The black dashed lines in **e** indicate the latitude of the sills, thus separating the two main regions of convection. Significance is assessed as in Fig. 12b

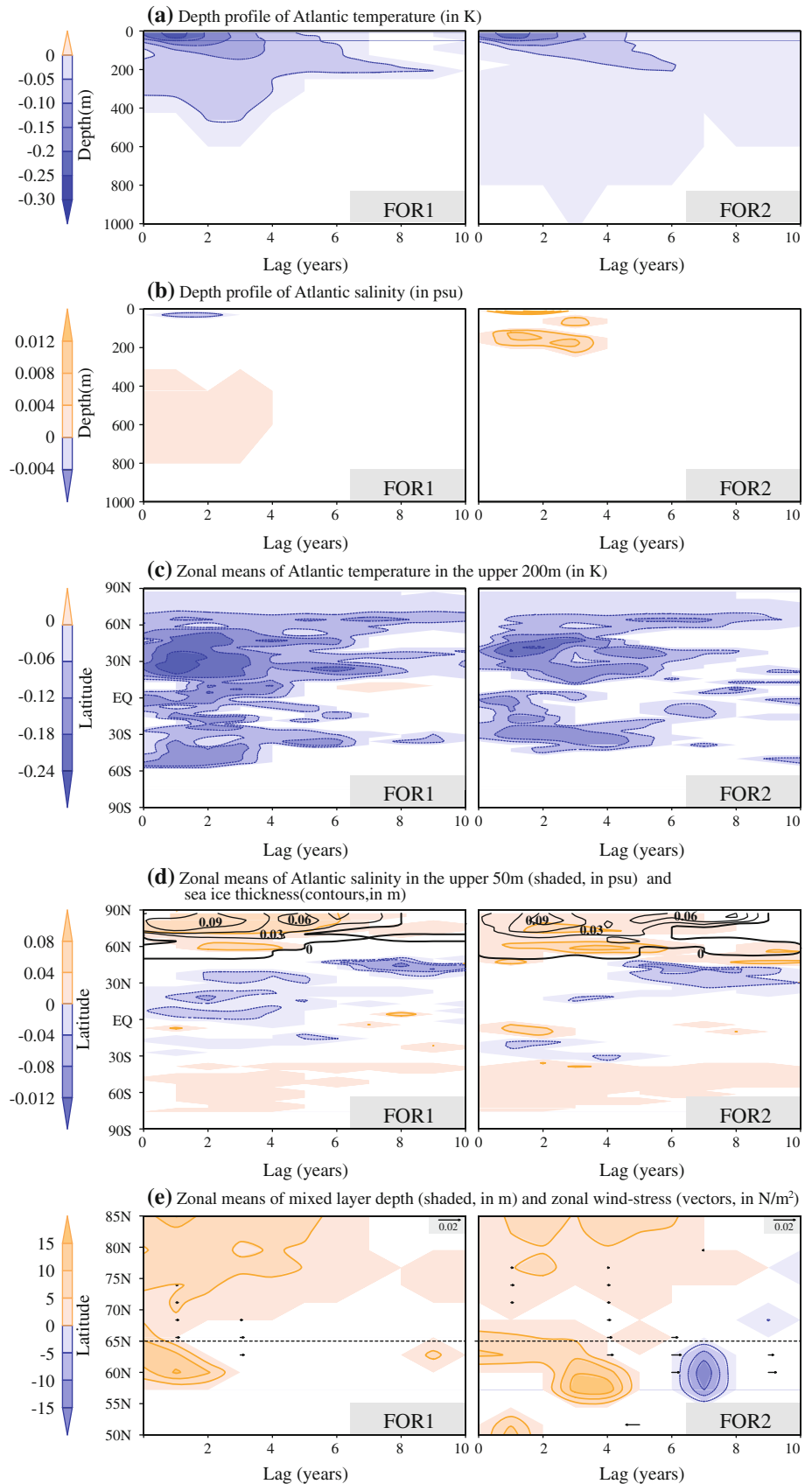
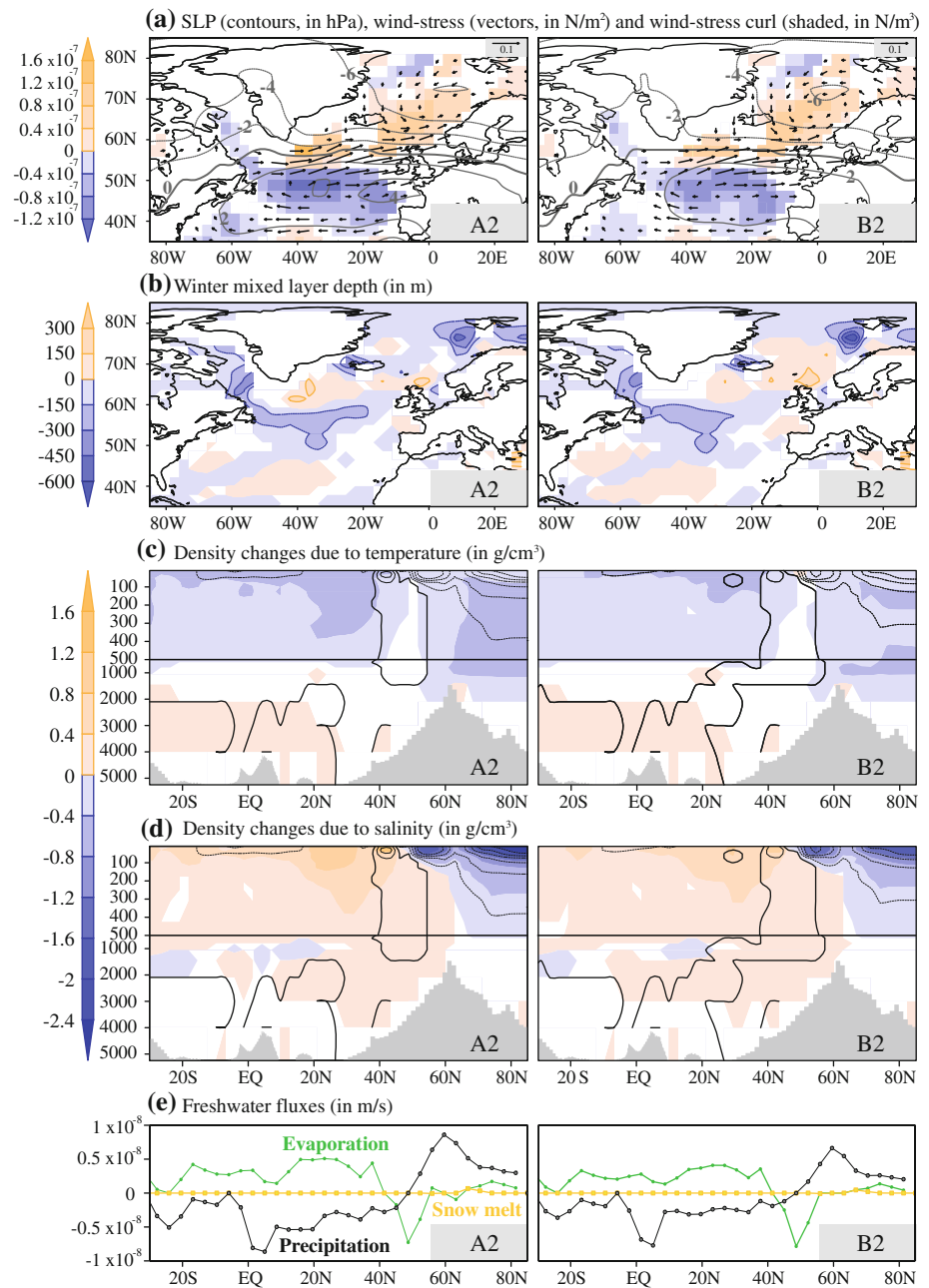


Fig. 15 Difference between the climatological mean of different quantities in the period 2070–2100 of the future scenarios A2 (left) and B2 (right) and the preindustrial era (1100–1850) in FOR1. The variables explored are: **a** SLP (contours, in hPa), wind-stress (vectors, in N/m^2) and wind-stress curl (shaded, in N/m^3), **b** winter mixed layer depth (in m), **c** density changes (in g/cm^3) due to temperature, **d** density changes (in g/cm^3) due to salinity, **e** freshwater fluxes (in m/s) related to precipitation (black line), evaporation (green line) and snow melt (yellow line). Note that positive precipitation and snow melt relate to freshwater fluxes from the atmosphere to the ocean, while positive evaporation relates to freshwater fluxes from the ocean to the atmosphere. Black contours in panels **c**, **d** account for total changes in density (contour interval is 0.4 g/cm^2). The zero lines are represented as a thick contours. Significance is assessed like in Fig. 12c



6.3 The fingerprint of increasing GHGs

The large sensitivity of climate models to increasing GHGs emerges from the fact that its radiative effect is both strong (unlike for the solar forcing) and long-lasting (unlike for volcanic aerosols). Most climate change projections are characterised by a decrease in surface density in the North Atlantic, due to the combined effect of increased precipitation and surface warming (Rahmstorf and Ganopolski 1999; Cubasch et al. 2001; Gregory et al. 2005; Meehl et al. 2007). In response to the lighter waters NADW formation is weakened, and therefore the AMOC.

The impact of increasing GHG concentrations is analysed computing the difference in means between the last 31 years of the future projections (when the GHG forcing is larger) and the preindustrial era, that can be assumed to incorporate only natural forcing changes. Significance is assessed by comparing these differences to the percentiles 2.5th and 97.5th of a new preindustrial ensemble. This time, each member is calculated as the average of the preindustrial anomalies in a period of 31 years. There is a total of 721 different such periods throughout the preindustrial era. Due to the strong forcing, most of the differences turn out to be significant (Figs. 12c, 15). By the end

of the twenty-first century both scenario simulations (A2 and B2) show a substantial weakening of the AMOC cell with respect to the mean preindustrial values (Fig. 12). This weakening is more prominent in the deep ocean, with a maximum decrease of ~ 14 Sv around 3000m depth that leads to a shoaling of the whole AMOC cell that is compatible with results from other climate change simulations (Manabe and Stouffer 1994; Schaeffer et al. 2004; Bryan et al. 2006; Drijfhout et al. 2008). Also relevant is a slowdown of the GSR overflow.

To understand these changes, other quantities are investigated. The main response in SLP is shown in Fig. 15a, characterised by a dipole-like structure that resembles a positive phase of the NAO. Other global warming runs also predict a positive increase in the NAO with increasing GHG concentrations (Stephenson et al. 2006; Meehl et al. 2007). As already shown in Sect. 4, positive NAO phases go along with increased Ekman pumping and zonal wind stress south of Cape Farewell, both countering the weakening effect of the lighter surface conditions on convection activity. As a result, there is a small increase in the mixed layer depth at the western Irminger Sea (Fig. 15b). Other regions, like the Inner Labrador or the Nordic Seas, show a general weakening of convection (Fig. 15b). However, these changes seem insufficient to explain the major reduction in the AMOC strength.

We turn our attention to the basin-scale changes in density, separating the contributions from temperature and salinity. Under climate change conditions the Atlantic ocean experiences a general warming which translates into negative density anomalies all across the basin, more important in the Nordic Seas and at tropical latitudes (Fig. 15c). However, the main changes in density are largely related to salinity (Fig. 15d). In the Tropics, surface salinity increases through reduced precipitation and enhanced evaporation (Fig. 15e), canceling out the effect of the local warming on density. Note that positive freshwater fluxes (from the atmosphere to the ocean) are related to reduced evaporation and increased snow melt and precipitation. In contrast, North Atlantic salinity decreases considerably in response to a general increase in precipitation, a local decrease of evaporation near 50°N, and a lesser contribution from snow melt at higher latitudes. In the Nordic seas, the combined effect of both salinity and temperature adds up to produce a local drop in density. The lighter waters north of the sill, plus the small net changes in the Tropics are associated with a sizeable reduction of the meridional density gradient (black contours in Fig. 15c, d), that favours a weakening of the GSR overflow as well as of the AMOC (Thorpe et al. 2001). Therefore, results highlight the crucial role of salinity and the water cycle to drive the major changes in the Atlantic.

7 Conclusions and discussion

The present paper focuses on the analysis of the AMOC variability in an unforced present-day control run, two forced runs for the last millennium, and two IPCC scenarios. The evolution of the MOI throughout the millennial simulations shows that most of the AMOC variability takes place at multidecadal time scales both in the control and the forced runs. The main mechanisms responsible for the overturning variability in two different time scales have been identified and analysed. In the high-frequency the local overturning variability is found to be forced by different wind regimes at different latitudes, largely driven by three well-known teleconnection patterns: ENSO, NAO, EA. The analysis in the low frequencies underlines the role of Labrador and Irminger convection in the North Atlantic deep water formation, and thereby in the variability of the overturning circulation. The delayed influence of the NAO in the forced runs, leading convection changes by one year, is in line with other model simulations (Delworth and Greatbatch 2000; Eden and Willebrand 2001; Bentsen et al. 2004; Guemas and Salas-Méla 2008) and observational analyses (Dickson et al. 1996; Curry et al. 1998). The balance of evidence from available modelling and observational studies suggests that both heat fluxes changes and wind-stress variations are important means of conveying NAO variability to influence AMOC variations in a wide range of frequencies. Although our results emphasise more the role of wind-stress changes, anomalous heat flux forcing can also play an important contribution as suggested in other studies (Delworth and Greatbatch 2000; Eden and Willebrand 2001). The importance of persistent anomalous heat fluxes for AMOC variability and predictability in the ECHO-G model is analysed in a companion paper (Ortega et al. 2011).

The influence of the radiative forcing has been also evaluated. The first notable impact is an interdecadal modulation on the position of the AMOC maximum. Several processes can contribute to this modulation. For example, the existence of a GSR overflow in the forced runs, which is not resolved in CTRL, can explain the occurrence of the maximum at deeper levels in FOR1 and FOR2. Also, externally forced changes in the main teleconnection patterns, either in their prevailing frequencies or in their spatial features, can modify the location at which AMOC maxima occurs. Indeed, an enhanced role of the NAO forcing has been identified in both FOR1 and FOR2. The meridional pressure gradient in the North Atlantic is found to increase in response to the forcing, thus leading to stronger wind forcing over the Labrador Sea. Potential changes on ENSO and EA variability have not been specifically analysed, and could also impact AMOC variability at high-frequencies. In a final step, the isolated influence of

the three forcing factors has been investigated. Only the GHG concentrations have a strong impact on the AMOC strength. The two forced simulations exhibit a substantial decrease in the overturning strength starting in the Industrial Era and continuing in the future scenario simulations (Fig. 3), well below the range of natural AMOC variability simulated for the past millennium and the control simulation. This final weakening is associated with a reduced meridional density gradient and with decreased convection in the North Atlantic, both mainly responding to changes in the atmospheric water transport. In contrast, the forcing due to insolation and volcanic aerosols produces minor changes in salinity and moderate shallow changes in temperature. In the case of solar irradiance, these changes occur far from the Labrador and Irminger convection regions, and thereby the impact on the AMOC is negligible. More interestingly, the upper cooling following the main volcanic eruptions is accompanied by a rise in surface salinity, both therefore contributing to a small general increase of convection in the North Atlantic. This produces a minor strengthening of the AMOC cell, in particular if compared to results from other models (Stenchikov et al. 2009; Ottera et al. 2010).

The response of the major circulation patterns to the forcing and their potential impact on the AMOC have been also assessed. The main response is a clear tendency to positive NAO phases with the increasing GHGs, previously identified in Zorita et al. (2005). However, it has a negligible effect on the AMOC, whose response is mainly dominated by density changes. An important caveat to consider is the coarse vertical resolution in the atmospheric component of ECHO-G, with only five levels in the stratosphere. In fact, models lacking a realistic representation of the stratosphere, both chemical and dynamical, tend to underestimate the impact of the radiative forcing on high-latitude atmospheric circulation (Knutson et al. 2006; Miller et al. 2006; Stenchikov et al. 2006). This implies that the NAO sensitivity to the forcing might be underestimated in ECHO-G, which would have potential consequences for the interpretation of the AMOC response.

In the analysis of the response to the forcing, another source of uncertainty resides on the reconstructions considered. The range of solar variability between the Maunder Minimum and the present climate has been reduced in a factor of 2–4 by recent estimates (Wang et al. 2005; Krivova et al. 2007; Tapping et al. 2007), as compared to the ones employed herein (Lean et al. 1995; Crowley 2000). These new estimates should significantly weaken the global response in temperature, and thus reduce the influence on convection and the sensitivity of the AMOC. Likewise, the ocean impact of volcanic aerosols might be underestimated in the model because of the low-resolution, the simplified physics and the smoothing effect of

composite averaging. For example, other works analysing large individual eruptions (e.g. Tambora, Pinatubo, Krakatoa) find a deep cooling signal persisting for several decades (Gleckler et al. 2006a, b), that may have a large impact on the AMOC (Stenchikov et al. 2009). Also, the Bergen climate model, with a higher resolved atmospheric component, shows a remarkable AMOC strengthening caused by the direct radiative cooling, but also through a volcanic modulation of the NAO (Ottera et al. 2010).

Yet, one of the main open questions is to determine whether and how the AMOC responds to the increasing GHG concentrations, given the uncertainty in the future emissions (Nakicenovic and Swart 2000) and the complexity of the feedback mechanisms involved. Indeed, in response to identical future scenarios, different models simulate somewhat different changes (Schmittner et al. 2005; Schneider et al. 2007). The multi-model spread is rather large, but no model predicts an abrupt change or a complete shutdown of the AMOC within the next century (Meehl et al. 2007). Our results are in line with these findings. Finally, the potential effect of other forcing factors is discussed. None of the forced simulations incorporate the influence from sulphate aerosols, which probably results in an overestimation of the AMOC weakening (Delworth and Dixon 2006). Changes in the vegetation cover, which have been found to attenuate the industrial warming trend in other GCM simulations (Bauer et al. 2003), were not included either. The associated cooling could also influence the variability of the AMOC, but the nature and magnitude of this change remains still uncertain.

The processes and interactions described above are specific to this model and thus are influenced by its particular biases. The representation of the ocean circulation, and in particular of the western boundary currents, is influenced by the use of flux corrections, that reach maximum values in their vicinity, and also in the upwelling regions at the western coasts of the continents. Maps showing the spatial distribution of these fluxes, as estimated for a previous simulation in ECHO-G, can be found in Legutke and Maier-Reimer (1999). The absence of momentum flux adjustments and the time invariant nature of the corrections minimise their potential influence on the mechanisms described, given the prevailing role of the wind forcing to drive the AMOC changes. Furthermore, an accurate representation of ocean dynamics and thereby of deep water formation is hindered both by the coarse resolution and by the fact that ECHO-G is not eddy-resolving. Therefore, the model misrepresents quantities as the overflow through the Greenland-Scotland Ridge (0–3 Sv, Fig. 2), or the intensity of the subpolar gyre (~ 15 Sv, not shown), both below the range of observational estimates of 6 Sv (Olsen et al. 2008) and 20–33 Sv (Clarke 1984),

respectively. Likewise, deep convection is generally weak in the North Atlantic as compared to observations (Marshall and Schott 1999), and locally overestimated over the Central Irminger Sea. As a result of the different unresolved processes, the typical timescales of the mechanisms described herein might be rather long. Indeed, latitudinal propagation of overturning anomalies is significantly faster in eddy-permitting models, due to a better representation of fast boundary waves (Getzlaff et al. 2005). Perhaps more importantly, the little sensitivity of the AMOC to the moderate forcing (e.g. solar irradiance and volcanic aerosols) can be fostered by misrepresented deep convection in the model, given the lesser role that the high latitudes (more sensitive to the forcing) are found to play on deep water formation. Therefore, evaluating in other models the validity of these results is an important subject for further work.

Acknowledgments This work was possible thanks to the funding by the MCINN projects CGL2005-06097 and CGL2008-06558-C02-C01/CLI, the MARM project 200800050084028 and also by the European Community's 7th framework programme (FP7/2007–2013) under grant agreement No. GA212643 (THOR: "Thermohaline Overturning circulation at Risk?", 2008–2012). The authors are grateful to the four anonymous reviewers for their helpful comments and suggestions that helped improve the current version of the manuscript. We would also like to thank Myriam Khodri and Didier Swingedouw for their valuable advice.

References

- Bacon S, Gould WJ, Jia Y (2003) Open convection in the Irminger Sea. *Geophys Res Lett* 30:1246
- Baehr J, Keller K, Marotzke J (2008) Detecting potential changes in the meridional overturning circulation at 26°N in the Atlantic. *Clim Change* 91(1–2):11–27, doi:10.1007/s10584-006-9153-z
- Barnston AG, Livezey RE (1987) Classification, seasonality and persistence of low-frequency atmospheric circulation patterns. *Monthly Weather Rev* 115:1083–1126
- Bauer E, Claussen M, Brovkin V, Huenerbein A (2003) Assessing climate forcings of the earth system for the past millennium. *Geophys Res Lett* 30:1276, doi:10.1029/2002GL016.639
- Beltrami H, González-Rouco JF, Stevens MB (2006) Subsurface temperatures during the last millennium: model and observation. *Geophys Res Lett* 33:L09,705, doi:10.1029/2006GL026050
- Bentsen M, Drange H, Furevik T, Zhou T (2004) Simulated variability of the Atlantic meridional overturning circulation. *Clim Dyn* 22:701–720
- Bloomfield P (1976) *Fourier analysis of time series: an introduction*. Wiley, New York
- Bretherton C, Widmann M, Dymnikov V, Wallace J, Bladé I (1999) The effective number of spatial degrees of freedom of a time-varying field. *J Clim* 12(7):1990–2009
- Bryan F, Danabasoglu G, Nakashiki N, Yoshida Y, Kim DH, Tsutsui J, Doney SC (2006) Response of the north Atlantic thermohaline circulation and ventilation to increasing carbon dioxide in ccsm3. *J Clim* 19:2382–2397
- Cabanes C, Lee T, Fu LL (2008) Mechanisms of interannual variations of the meridional overturning circulation of the North Atlantic Ocean. *J Phys Oceanogr* 38:467–480
- Clarke RA (1984) Transport through the Cape Farewell–Flemish Cap section. *Rapp P V Reun Cons Int Explor Mer* 185:120–130
- Crowley TJ (2000) Causes of climate change over the past 1000 years. *Science* 289:270–277
- Cubasch U, Voss R, Hegerl GC, Waszkewitz J, Crowley TJ (1997) Simulation of the influence of solar radiation variations on the global climate with an ocean-atmosphere general circulation model. *Clim Dyn* 13:757–767
- Ubasch U, Meehl G, Boer G, Stouffer R, Dix M, Noda A, Senior C, Raper S, Yap K (2001) Projections of future climate change. In: Houghton JT et al. (eds) *Climate change 2001: the scientific basis: contribution of working group I to the third assessment report of the intergovernmental panel on climate change*. Cambridge University Press, New York, pp 525–582
- Curry R, McCartney M, Joyce T (1998) Oceanic transport of subpolar climate signals to mid-depth subtropical waters. *Nature* 391:575–577
- Delworth T, Dixon K (2006) Have anthropogenic aerosols delayed a greenhouse gas-induced weakening of the North Atlantic thermohaline circulation? *grl* 33:L02,606, doi:10.1029/2005GL024,980
- Delworth T, Stouffer R, Dixon K, Spelman MJ, Knutson T, Broccoli A, Kushner P, Wetherald R (2002) Review of simulations of climate variability and change with the GFDL R30 coupled climate model. *cd* 19:555–574
- Delworth TL, Greatbatch RJ (2000) Multidecadal thermohaline circulation variability driven by atmospheric surface flux forcing. *J Clim* 13:1481–1495
- Delworth TL, Mann ME (2000) Observed and simulated multidecadal variability in the Northern Hemisphere. *Clim Dyn* 16:661–676
- Delworth TL, Manabe S, Stouffer RJ (1993) Interdecadal variations in the thermohaline circulation in a coupled ocean-atmosphere model. *J Clim* 6:1993–2011
- Deshayes J, Frankignoul C (2008) Simulated variability of the circulation in the North Atlantic from 1953 to 2003. *J Clim* 21:4919–4933
- Dickson R, Lazier J, Meincke J, Rhines P, Swift J (1996) Long-term coordinated changes in the convective activity of the North Atlantic. *Progress Oceanogr* 38:241–295
- Dong B, Sutton RT (2005) Mechanism of interdecadal thermohaline circulation variability in a coupled ocean-atmosphere GCM. *J Clim* 18:1117–1135
- Dong B, Sutton RT (2007) Enhancement of ENSO variability by a weakened Atlantic thermohaline circulation in a coupled GCM. *J Clim* 20:4920–4939
- Dong B, Sutton RT, Scaife AA (2006) Multidecadal modulation of El Niño–Southern Oscillation (ENSO) variance by Atlantic Ocean sea surface temperatures. *Geophys Res Lett* 33:L08,705, doi:10.1029/2006GL025,766
- Drijfhout S, Hazeleger W (2007) Detecting Atlantic MOC changes in an ensemble of climate change simulations. *JOC* 20:1571–1582
- Drijfhout SS, Hazeleger W, Selten F, Haarsma R (2008) Future changes in internal variability of the Atlantic meridional overturning circulation. *Clim Dyn* 30:407–419, doi:10.1007/s00,382-007-0297-y
- Eden C, Greatbatch RJ (2003) A damped decadal oscillation in the North Atlantic climate system. *J Clim* 16:4043–4060
- Eden C, Jung T (2001) North Atlantic interdecadal variability: oceanic response to the North Atlantic oscillation (1865–1997). *J Clim* 14:676–691
- Eden C, Willebrand J (2001) Mechanism of interannual to decadal variability of the North Atlantic circulation. *J Clim* 14:2266–2280
- Frankcombe LM, von der Heydt A, Dijkstra H (2010) North Atlantic multidecadal climate variability: an investigation of dominant time scales and processes. *J Clim* 23(13):3626–3638, doi:10.1175/2010JCLI3471.1

- Ganachaud A, Wunsch C (2000) Improved estimates of global ocean circulation, heat transport and mixing from hydrographic data. *Nature* 408:453–457
- Gates WL (1992) AMIP: the atmosphere model intercomparison project. Technical report 7, Program for Climate Model Diagnosis and Intercomparison, Lawrence Livermore National Laboratory, Livermore
- Getzlaff J, Böning C, Eden C, Biastoch A (2005) Signal propagation related to the north atlantic overturning. *Geophys Res Lett* 32:L09,602, doi:[10.1029/2004GL021002](https://doi.org/10.1029/2004GL021002)
- Gleckler P, AchutaRao K, Gregory J, Santer B, Taylor K, Wigley T (2006a) Krakatoa lives: the effect of volcanic eruptions on ocean heat content and thermal expansion. *Geophys Res Lett* 33(L17):L17,702, doi:[10.1029/2006GL026771](https://doi.org/10.1029/2006GL026771)
- Gleckler PJ, Wigley T, Santer B, Gregory J, AchutaRao K, Taylor KE (2006b) Krakatoa's signature persists in the ocean. *Nature* 439:675
- González-Rouco FJ, Beltrami H, Zorita E, von Storch H (2006) Simulation and inversion of borehole temperature profiles in surrogate climates: spatial distribution and surface coupling. *Geophys Res Lett* 33:L01,703, doi:[10.1029/2005GL024693](https://doi.org/10.1029/2005GL024693)
- González-Rouco FJ, Beltrami H, Zorita E, Stevens MB (2009) Borehole climatology: a discussion based on contributions from climate modeling. *Clim Past* 5:97–127
- González-Rouco JF, von Storch H, Zorita E (2003a) Deep soil temperature as proxy for surface air-temperature in a coupled model simulation of the last thousand years. *Geophys Res Lett* 30:2116–2119
- González-Rouco JF, Zorita E, Cubasch U, von Storch H, Fisher-Bruns I, Valero F, Montavez JP, Schlese U, Legutke S (2003b) Simulating the climate since 1000 AD with the AOGCM ECHO-G. *ESA SP* 535:329–338
- Goosse H, Crowley T, Zorita E, Ammann C, Renssen H, Driesschaert E (2005) Modelling the climate of the last millennium: what causes the differences between simulations?. *Geophys Res Lett* 32:L06,710
- Gouirand I, Moron V, Zorita E (2007a) Teleconnections between enso and north atlantic in an echo-g simulation of the 1000–1990 period. *Geophys Res Lett* 34:L06,705, doi:[10.1029/2006GL028852](https://doi.org/10.1029/2006GL028852)
- Gouirand I, Moberg A, Zorita E (2007b) Climate variability in scandinavia for the past millennium simulated by an atmosphere-ocean general circulation model. *Tellus* 59A:30–49
- Gregory JM, Dixon KW, Stouffer RJ, Weaver AJ, Driesschaert E, Eby M, Fichefet T, Hasumi H, Hu A, Jungclaus JH, Kamenkovich IV, Levermann A, Montoya M, Murakami S, Nawrath S, Oka A, Sokolov AP, Thorpe RB (2005) A model intercomparison of changes in the Atlantic thermohaline circulation in response to increasing atmospheric CO₂ concentration. *Geophys Res Lett* 32:L12,703, doi:[10.1029/2005GL023209](https://doi.org/10.1029/2005GL023209)
- Guemas V, Salas-Méllia D (2008) Simulation of the Atlantic meridional overturning circulation in an atmosphere-ocean global coupled model. Part I: a mechanism governing the variability of ocean convection in a preindustrial experiment. *Clim Dyn* 31:29–48
- Hansen B, Østerhus S (2000) North atlantic-nordic seas exchanges. *Progress Oceanogr* 45:109–208
- Hasselmann K (1976) Stochastic climate models, part i: theory. *Tellus* 28:473–485
- Hawkins E, Sutton R (2007) Variability of the atlantic thermohaline circulation described by three-dimensional empirical orthogonal functions. *Clim Dyn* 29:745–762
- Hirschi JJM, Killworth PD, Blundell JR (2007) Subannual, seasonal, and interannual variability of the North Atlantic meridional overturning circulation. *J Phys Oceanogr* 37:1246–1265
- Hofer D, Raible CC, Stocker TF (2011) Variations of the atlantic meridional overturning circulation in control and transient simulations of the last millennium. *Clim Past* 7:133–150, doi:[10.5194/cp-7-133-2011](https://doi.org/10.5194/cp-7-133-2011)
- Jansen E, Overpeck J, Briffa K, Duplessy JC, Joos F, Masson-Delmotte V, Olago D, Otto-Bliensner B, Peltier W, Rahmstorf S, Ramesh R, Raynaud D, Rind D, Solomina O, Villalba R, Zhang D (2007) Climate change 2007: the physical science basis. Contribution of Working Group I to the Fourth Assessment Report of the Intergovernmental Panel on Climate Change, edited by S. Solomon and D. Qin and M. Manning and Z. Chen and M. Marquis and K.B. Averyt and M. Tignor and H.L. Miller, Cambridge University Press, Cambridge
- Jungclaus JH, Haak H, Latif M, Mikolajewicz U (2005) Arctic-North Atlantic interactions and multidecadal variability of the meridional overturning circulation. *J Clim* 18:4013–4031
- Keenlyside N, Latif M, Jungclaus J, Kornbluh L, Roeckner E (2008) Advancing decadal-scale climate prediction in the North Atlantic sector. *Nature* 453:84–88, doi:[10.1038/nature06921](https://doi.org/10.1038/nature06921)
- Kerr R (2000) A North Atlantic climate pacemaker for the centuries. *Science* 288:1984–1986
- Knight JR, Allan RJ, Folland CK, Vellinga M, Mann ME (2005) A signature of persistent natural thermohaline circulation cycles in observed climate. *Geophys Res Lett* 32:L20,708, doi:[10.1029/2005GL024233](https://doi.org/10.1029/2005GL024233)
- Knight JR, Folland CK, Scaife AA (2006) Climate impacts of the atlantic multidecadal oscillation. *Geophys Res Lett* 33:L17,706
- Knutson T, Delworth T, Dixon K, Held I, Lu J, Ramaswamy V, Schwarzkopf M, Stenchikov G, Stouffer R (2006) Assessment of twentieth-century regional surface temperature trends using the gfdl cm2 coupled models. *J Clim* 19(9):1624–1651
- Krivova N, Balmaceda L, Solanki S (2007) Reconstruction of solar total irradiance since 1700 from the surface magnetic flux. *Astron Astrophys* 467:335–346, doi:[10.1051/0004-6361:20066725](https://doi.org/10.1051/0004-6361:20066725)
- Kushnir Y (1994) Interdecadal variations in North Atlantic sea surface temperature and associated atmospheric conditions. *J Clim* 7:141–157
- Latif M, Botzet M, Esch M, Haak H, Hagemann S, Jungclaus J, Legutke S, Marsland S, Mikolajewicz U (2004) Reconstructing, monitoring, and predicting multidecadal-scale changes in the North Atlantic thermohaline circulation with sea surface temperature. *J Clim* 17:1605–1614
- Lean J, Beer J, Bradley R (1995) Reconstruction of solar irradiance since 1610: Implications for climate change. *Geophys Res Lett* 22:3195–3198
- Legutke S, Maier-Reimer E (1999) Climatology of the HOPE-G global ocean general circulation model. Technical report 21, DKRZ, Hamburg, Germany, doi:[10.2312/WDCC/DKRZ_Report_No21](https://doi.org/10.2312/WDCC/DKRZ_Report_No21)
- Legutke S, Voss R (1999) The hamburg atmosphere-ocean coupled circulation model echo-g. Technical report 18, DKRZ, Hamburg, Germany
- Levitus S, Burgett R, Boyer TP (1994) World Ocean Atlas 1994, vol 3, Salinity and vol 4, Temperature. Technical report, National Environmental Satellite, Data, and Information Service, Washington, DC (United States)
- Manabe S, Stouffer RJ (1994) Multiple-century response of a coupled ocean-atmosphere model to an increase of atmospheric carbon dioxide. *J Clim* 7:5–23
- Marotzke J, Stone P (1995) Atmospheric transports, the thermohaline circulation, and flux adjustments in a simple coupled model. *J Phys Oceanogr* 25:1350–1364
- Marshall JC, Schott F (1999) Open ocean convection: observations, theory and models. *Rev Geophys* 37-1:1–64

- Meehl GA, Stocker TF, Collins WD, Friedlingstein P, Gaye AT, Gregory JM, Kitoh A, Knutti R, Murphy JM, Noda A, Raper SCB, Watterson IG, Weaver AJ, Zhao ZC (2007) Global climate projections. In: *Climate change 2007: the physical science basis. Contribution of working group I to the fourth assessment report of the intergovernmental panel on climate change*. Cambridge University Press, Cambridge
- Mignot J, Frankignoul C (2005) The variability of the Atlantic meridional overturning circulation, the North Atlantic oscillation, and the El Niño-Southern oscillation in the Bergen climate model. *J Clim* 18:2361–2375
- Miller R, Schmidt G, Shindell D (2006) Forced annular variations in the 20th century intergovernmental panel on climate change fourth assessment report models. *J Geophys Res* 111:D18,101
- Min S, Legutke S, Hense A, Kwon W (2005a) Internal variability in a 1000-yr control simulation with the coupled climate model ECHO-G-I. Near surface temperature, precipitation and sea level pressure. *Tellus* 57A:605–621
- Min S, Legutke S, Hense A, Kwon W (2005b) Internal variability in a 1000-yr control simulation with the coupled climate model ECHO-G-II. El Niño Southern Oscillation and North Atlantic Oscillation. *Tellus* 57A:622–640
- Moore GWK (2003) Gale force winds over the Irminger Sea to the east of Cape Farewell, Greenland. *Geophys Res Lett* 30:1894, doi:10.1029/2003GL018,012
- Msadek R, Frankignoul C (2009) Atlantic multidecadal oceanic variability and its influence on the atmosphere in a climate model. *Clim Dyn* 33:45–62, doi:10.1007/s00382-008-0452-0
- Nakicenovic N, Swart R (eds) (2000) *IPCC special report on emissions scenarios*. Cambridge University Press, Cambridge
- Nakicenovic N, Alcamo J, Davis G, de Vries B, Fenhann J, Gaffin S, Gregory K, Grubler A, Jung TY, Kram T, Rovere ELL, Michaelis L, Mori S, Morita T, Pepper W, Pitcher H, Price L, Riahi K, Roehrl A, Rogner HH, Sankovski A, Schlesinger M, Shukla P, Smith S, Swart R, van Rooijen S, Victor N, Dadi Z (2000) *Special Report on Emissions Scenarios*. Cambridge University Press, Cambridge
- Olsen SM, Hansen B, Quadfasel D, Østerhus S (2008) Observed and modelled stability of overflow across the greenland–scotland ridge. *Nature* 455(7212):519–522, doi:10.1038/nature07302
- Orsi AH, Johnson GC, Bullister JL (1999) Circulation, mixing, and production of Antarctic bottom water. *Progress Oceanogr* 43:55–109
- Ortega P, Hawkins E, Sutton RT (2011) Processes governing the predictability of the Atlantic meridional overturning circulation in a coupled GCM. *Clim Dyn* (accepted), doi:10.1007/s00382-011-1025-1
- Osborn TJ, Raper SCB, Briffa KR (2006) Simulated climate change during the last 1000 years: comparing the ECHO-G general circulation model with the MAGICC simple climate model. *Clim Dyn* 27:185–197, doi:10.1007/s00382-006-0129-5
- Ottera OH, Bentsen M, Drange H, Suo L (2010) External forcing as a metronome for atlantic multidecadal variability. *Nat Geosci* 3:688–694, doi:10.1038/NNGEO955
- Peng S, Robinson W, Li S, Hoerling M (2005) Tropical atlantic sst forcing of coupled north atlantic seasonal responses. *J Clim* 18(3):480–496
- Pickart RS, Spall MA, Ribergaard MJ, Moore GWK, Milliff RF (2003) Deep convection in the Irminger Sea forced by the Greenland tip jet. *Nature* 424:152–156
- Rahmstorf S, Ganopolski A (1999) Long-term global warming scenarios computed with an efficient coupled climate model. *Clim Change* 43:353
- Rind D, Shindell D, Perlwitz J, Lerner J, Lonergan P, Lean J, McLinden C (2004) The relative importance of solar and anthropogenic forcing of climate change between the maunder minimum and the present. *J Clim* 17:906–929
- Rodwell M, Rowell D, Folland C (1999) Oceanic forcing of the wintertime north atlantic oscillation and european climate. *Nature* 398(6725):320–323
- Roeckner E, Arpe K, Bengtsson L, Christoph M, Claussen M, Dumenil L, Esch M, Giorgetta M, Schlese U, Schulzweida U (1996) The atmospheric general circulation model ECHAM4: model description and simulation of present-day climate. Technical report 218, Max-Planck-Institut fuer Meteorologie, Hamburg, Germany
- Schaeffer M, Selten F, Opsteegh J, Goosse H (2004) The influence of ocean convection patterns on high-latitude climate projections. *J Clim* 17:4316–4329
- Schmittner A, Latif M, Schneider B (2005) Model projections of the North Atlantic thermohaline circulation for the 21st century assessed by observations. *Geophys Res Lett* 32:L23,710, doi:10.1029/2005GL024,368
- Schneider B, Latif M, Schmittner A (2007) Evaluation of different methods to assess model projections of the future evolution of the atlantic meridional overturning circulation. *J Clim* 20:2121–2132, doi:10.1175/JCLI4128.1
- Sedláček J, Mysak LA (2009a) A model study of the little ice age and beyond: changes in ocean heat content, hydrography and circulation since 1500. *Clim Dyn* 33:461–475, doi:10.1007/s00382-008-0503-6
- Sedláček J, Mysak LA (2009b) Sensitivity of sea ice to wind-stress and radiative forcing since 1500: a model study of the little ice age and beyond. *Clim Dyn* 32(6):817–831, doi:10.1007/s00382-008-0406-6
- Shindell D, Schmidt G, Mann M, Rind D, Waple A (2001) Solar forcing of regional climate change during the maunder minimum. *Science* 294:2149–2152, doi:10.1126/science.1064363
- Stenchikov G, Hamilton K, Stouffer R, Robock A, Ramaswamy V, Santer B, Graf H (2006) Arctic oscillation response to volcanic eruptions in the ipcc ar4 climate models. *J Geophys Res* 111:D07,107, doi:10.1029/2005JD006286
- Stenchikov G, Delworth T, Ramaswamy V, Stouffer RJ, Wittenberg A, Zeng F (2009) Volcanic signals in oceans. *J Geophys Res Atmos* 114:D16,104, doi:10.1029/2008JD011673
- Stendel M, Mogensen I, Christensen J (2006) Influence of various forcings on global climate in historical times using a coupled atmosphere–ocean general circulation model. *Clim Dyn* 26:1–15, doi:10.1007/s00382-005-0041-4
- Stephenson D, Pavan V, Collins M, Junge M, Quadrelli R (2006) North atlantic oscillation response to transient greenhouse gas forcing and the impact on european winter climate: a cmip2 multi-model assessment. *Clim Dyn* 27:401–420
- Stevens MB, Smerdon JE, González-Rouco JF, Stieglitz M, Beltrami H (2007) Effects of bottom boundary condition placement on subsurface heat storage: implications for climate model simulations. *Geophys Res Lett* 34:L02,702, doi:10.1029/2006GL028546
- von Storch H, Zorita E, Jones JM, Dimitriev Y, Gonzalez-Rouco F, Tett SFB (2004) Reconstructing past climate from noisy data. *Science* 306:679–682, doi:10.1126/science.1096109
- Sutton RT, Hodson DLR (2003) Influence of the ocean on North Atlantic climate variability 1871–1999. *J Clim* 16:3296–3313
- Swingedouw D, Terray L, Cassou C, Voldoire A, Salas-Mélia D, Servonnat J (2010) Natural forcing of climate during the last millennium: fingerprint of solar variability. *Clim Dyn* 36:1349–1364, doi:10.1007/s00382-010-0803-5
- Talley LD (2003) Shallow, intermediate, and deep overturning components of the global heat budget. *J Phys Oceanogr* 33: 530–560

- Talley LD, Reid JL, Robbins PE (2003) Data-based meridional overturning streamfunctions for the global ocean. *J Clim* 16:3213–3226
- Tapping KF, Boteler D, Charbonneau P, Crouch A, Manson A, Paquette H (2007) Solar magnetic activity and total irradiance since the maunder minimum. *Solar Phys* 246:309–326, doi: [10.1007/s11207-007-9047-x](https://doi.org/10.1007/s11207-007-9047-x)
- Thorpe RB, Gregory JM, Johns TC, Wood RA, Mitchell JFB (2001) Mechanisms determining the Atlantic thermohaline circulation response to greenhouse gas forcing in a non-flux-adjusted coupled climate model. *J Clim* 14:3102–3116
- Timmermann A, Latif M, Voss R, Grötzner A (1998) Northern hemispheric interdecadal variability: a coupled air-sea mode. *J Clim* 11:1906–1931
- Timmermann A, Okumura Y, An SI, Clement A, Dong B, Guilyardi E, Hu A, Jungclaus JH, Renold M, Stocker TF, Stouffer RJ, Sutton R, Xie SP, Yin J (2007) The influence of a weakening of the Atlantic meridional overturning circulation on ENSO. *J Clim* 20:4489–4919
- Trenberth KE, Caron JM (2001) Estimates of meridional atmosphere and ocean heat transport. *Clim Dyn* 14:3433–3443
- Trenberth KE, Shea DJ (1987) On the evolution of the southern oscillation. *Monthly Weather Rev* 115:3078–3096
- Vellinga M, Wu P (2004) Low-latitude freshwater influence on centennial variability of the Atlantic thermohaline circulation. *J Clim* 17:4498–4511
- Wallace J, Gutzler D (1981) Teleconnections in the geopotential height field during the northern hemisphere winter. *Monthly Weather Rev* 109:784–812
- Wang Y, Lean J, Sheeley N (2005) Modeling the sun’s magnetic field and irradiance since 1713. *Astrophys J* 625:522–538
- Weaver AH, Valcke S (1998) On the variability of the thermohaline circulation in the gfdl coupled model. *J Clim* 11:759–767
- Wolff JO, Maier-Reimer E, Legutke S (1997) The Hamburg ocean primitive equation model. Technical report 13, DKRZ, Hamburg, Germany
- Wu P, Gordon C (2002) Oceanic influence on North Atlantic climate variability. *J Clim* 15:1911–1925
- Zorita E, González-Rouco JF, Legutke S (2003) Testing the Mann et al. (1999) approach to paleoclimate reconstructions in the context of a 1000-yr control simulation with the ECHO-G coupled climate model. *J Clim* 16:1378–1390
- Zorita E, von Storch H, González-Rouco FJ, U Cubasch JL, Legutke S, Fischer-Bruns I, Schlese U (2004) Climate evolution in the last five centuries simulated by an atmosphere-ocean model: global temperatures, the North Atlantic Oscillation and the Late Maunder Minimum. *Meteorol Z* 13(4):271–289
- Zorita E, González-Rouco JF, von Storch H, Montávez JP, Valero F (2005) Natural and anthropogenic modes of surface temperature variations in the last thousand years. *Geophys Res Lett* 32:L08,707
- Zorita E, Gonzalez-Rouco F, von Storch H (2007) Comments on “testing the fidelity of methods used in proxy-based reconstructions of past climate”. *J Clim* 20:3693–3698